Tectonic-sedimentary architecture of surficial deposits along the continental slope offshore Romania (North of the Viteaz Canyon, Western Black Sea): Impact on sediment instabilities

T. Marsset, G. Ballas, I. Munteanu, C. Aiken, G. Ion, M. Pitel-Roudaut, P. Dupont

Tectonic-sedimentary Architecture of Surficial Deposits along the Continental Slope Offshore Romania (North of the Viteaz Canyon, Western Black Sea): Impact on Sediment Instabilities

Marsset T.[a], Ballas G.[b], Munteanu I.[c], Aiken C.[a], Ion G.[d], Pitel-Roudaut M.[a], Dupont P.[a]

[a] Ifremer (Institut Français de Recherche pour l'Exploitation de la Mer), REM-GM, BP 70 29290 Plouzané, France

Corresponding author: tania.marsset@ifremer.fr

Tel: (33) 02 98 22 42 06

Fax: (33) 02 98 22 45 70

chastity.aiken@ifremer.fr

Mathilde.Pitel@ifremer.fr

pauline.dupont@ifremer.fr

[b] Géosciences Montpellier, Université de Montpellier, CNRS, France.

gregory.ballas@umontpellier.fr

[c] Faculty of Geology and Geophysics, University of Bucharest, 6 Traian Vuia St., Bucharest, Romania.

ioan.munteanu@unibuc.ro

[d] National Research and Development Institute for Marine Marine Geology and Geo-ecology - GeoEcoMar, 23-25, Dimitrie Onciul, Bucharest, Romania.

gion@geoecomar.ro

Abstract

The upper continental slope offshore Romania is a complex area hosting turbidite deposits, multiple types and ages of deep-seated faults, gas hydrates, gas-escape features, and numerous Mass Transport Deposits (MTDs). Multi-scale seismic data sets (2D-high-resolution and near-bottom very high-resolution) were used to study the interaction between such disparate geological features and determine their impact on slope stability.

At least five main paleo-valleys have been identified in the north of the Viteaz (Danube) canyon/valley. The most recent channelized systems linked to these valleys formed over a basal layer of MTDs. These MTDs are associated with an unconformity corresponding to the Base Neoeuxinian Sequence Boundary formed during the last major sea-level fall. This erosional surface shows scarp alignments that coincide with underlying faults. We argue that gravity-driven fault reactivation, with possible upward gas/fluid migration along these faults, is a determinant factor controlling sedimentary instabilities. Numerous MTDs are also observed during channel-levees building and reveal local sediment instabilities related to localized erosional process in the canyon. Finally, MTDs recorded within the upper draping unit, suggest that sediment instability also occurred during recent sea level highstand. Sediment pulse, seismicity, and gas hydrate dynamics can also play a determinant role in sediment instability throughout the sediment record.

Keywords:

Romanian continental slope; gas/gas hydrates; turbidite systems; sedimentary instabilities; gravitational faults.

1. Introduction

Sediment instabilities and gravity processes strongly affect continental slopes (Masson et al., 2006; Urlaub et al., 2013). Submarine landslides can involve large volumes of sediment (Tailling et al., 2014) and cause damage to telecommunication cables (Pope et al., 2017 and references therein) and seafloor structures (pipelines). They can also trigger tsunamis (Piper et al., 1999; Løvholt et al. 2020). Their role in sudden gas release and the related potential climate changes is also open to debate (Kennett et al., 2003; Maslin et al., 2004). Numerous features influence the generation or triggering of submarine landslides (Masson et al., 2006). Rapid sediment deposition and high sedimentation rates are well-known instability triggering mechanisms (Lee, 2005). The presence of gas in the sediments (Field and Barber, 1993; Garziglia et al., 2008; Riboulot et al., 2013), melting of gas hydrates (Sultan et al., 2004a, b; Pecher et al., 2005; Kim et al., 2013), and earthquakes can also lead to slope failure where the presence of a weak layer constitutes favourable conditions (Locat et al., 2014). The relative impacts of these factors are often inadequately constrained, mainly due to the difficulty in evaluating the role of each of these factors on the stacking pattern of sedimentary bodies.

Accordingly, this study aims to provide the detailed spatio-temporal tectonic and stratigraphic framework of an area located offshore Romania (NW Black Sea) where numerous sediment instabilities exist within surficial sediment deposits (Fig. 1; Fig. 2). Previous studies of this area have shown that the Mass Transport Deposits (MTDs) are located along the slope where numerous gas seeps and evidence of gas hydrates have been recorded (Popescu et al., 2007; Riboulot et al., 2017; Hillman et al., 2018; Ker et al., 2019). The work presented here is based on a multi-scale seismic database (mainly 2D-high-resolution and near-bottom very high-resolution). The data provide detailed stacking patterns of turbidite systems and MTDs, fault patterns, and their relationship with BSR (Bottom Simulating Reflector) and free gas extents. The main objective is to enhance the identification and definition of the relative importance of factors controlling sediment instability in this particular context of gas/gas-hydrate dynamics, multi-phased tectonics and sea-level fluctuations.

2. General setting and previous work

2.1 Geological setting

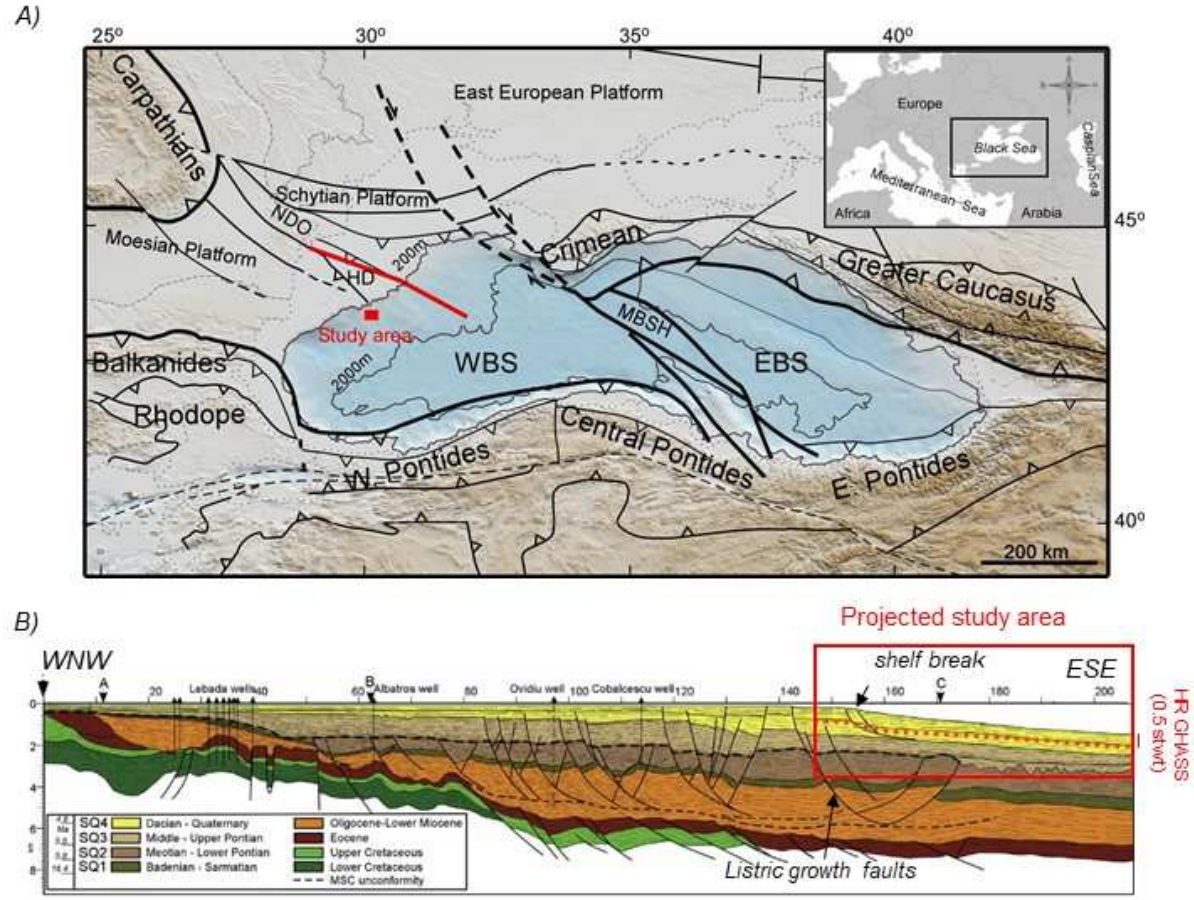

Fig. 1. Geological context of the Black Sea. A) Tectonic map (compilation from Finetti et al., 1988; Yilmaz et al., 1997; Nikishin et al., 2001; Dinu et al., 2005, 2018; Munteanu et al., 2011). Note the North Dobrogea orogenic belt (NDO), the Histria basin/trough well known in literature as Histria depression (HD over NDO) and the Eastern Black Sea (EBS), Western Black Sea (WBS), Mid Black Sea High (MBSH). The red line indicates the cross-section presented below. The red box indicates the location of the study area. B) Cross-section of the Romanian margin (from Matenco et al., 2016) showing the horsts and grabens resulting from the Mesozoic extensional phase and Cenozoic inversion. Note the gravitational

deformation of prograding sediments overlying late Oligocene layers and the associated faults. Note the listric growth faults below the present shelf break. The red box indicates the location of the study area on the upper continental slope.

The Western Black Sea is part of a back-arc domain that has experienced complex evolution with transition from an extensional setting (Cretaceous-early Eocene) to a contractional setting (late Eocene-Middle Miocene) during the northward Neotethyan subduction and collision (Letouzay et al., 1977; Zonenshain and Le Pichon, 1986; Finetti et al., 1988; Görür, 1988; Artyushkov, 1992; Robinson et al., 1996; Nikishin et al., 2001; Georgiev, 2012) (Fig. 1A). The rifting began during the Aptian and continued intermittently until the mid-Turonian (Krezsek et al., 2016). Continental break-up followed in the mid-Turonian caused by the regional uplift and erosion of the basin margin. Late Cretaceous- Paleogene times are marked by rift enlargement and eastward expansion and the development of the deep-sea basin (Munteanu et al., 2012). These two extensional stages led, in the northwestern area, to the formation of complex interplay between isolated blocks organized in horsts and grabens (Fig. 1B and red lines on Fig. 2), such as the Histria Basin (Fig. 1 and Fig. 2) which is located over the North Dobrogea Triassic-Jurassic orogenic belt (Dinu et al., 2005). Repeated periods of inversion from orogenic deformations (Balkans, Pontides, Crimean-Caucasus), are marked by the (re)activation of faults and associated folding during the late Cretaceous and Eocene-Miocene times (Hippolyte, 2002; Munteanu et al., 2011) (Fig. 1A).

Large thicknesses of sediments accumulated during the Pontian, i.e. Miocene-Pliocene transition from 6.04 to around 5 Ma (Dinu et al., 2003, 2005; Konerding et al., 2010; Tambrea, 2007) (Fig. 1B). At that time, which corresponds to the Messinian event, sea-level falls of debated amplitude (100-2300 m) led to large-scale erosion and significant progradation during the subsequent highstand (Hsü and Giovanoli, 1979; Gillet et al., 2007; Munteanu et al., 2012; Krezsek et al., 2016). The Dacian i.e. around 5 to 4 Ma, and the Romanian-Quaternary sediments reached thicknesses of up to 1200 m and 600 m respectively on the continental slope (Konerding et al., 2010) (Fig. 1B).

The high sediment load and high subsidence led to the development of gravitational faults (Konerding et al., 2010) (Fig. 1B) and overpressure of the Oligocene- early Miocene? sediments (Dinu et al., 2003; Bega and Ionescu, 2009), which provided the detachment level for shelf collapse during the Messinian large-scale sea level drop (Tambrea et al., 2002; Dinu et al., 2003; Munteanu et al., 2012; Schleder et al., 2016).

During the Plio-Quaternary, thick successions of MTDs and turbidite deposits took place in front of modern rivers (Munteanu et al., 2012; Matenco et al., 2016). The north-western Black Sea is currently dominated by a rather wide shelf (60-200 km) with a shelf break at 120 to 170 m water depth and canyon systems with large deep-sea fan complexes that mainly developed during sea-level Quaternary lowstands (Winguth et al., 2000; Popescu et al., 2002). The Danube delta system advanced into the Black Sea in the Romanian-Pleistocene in response to the increased sediment supply due to renewed uplift of the Carpathians (Matoshko et al., 2019; Krézsek and Olariu, 2021). The Danube river reached the Black Sea for the first time about 900 ka ago and subsequently built up the Danube fan (Winguth et al., 2000).

Note that several earthquakes were recorded in this area, especially from deeply rooted faults (Fig. 2, Table 1). The north-western Black Sea is also rich in hydrocarbon fields (oil, gas) (Kruglyakova et al., 2004; Georgiev, 2012), gas hydrates (Popescu et al., 2007; Merey and Sinayuc, 2016), and surficial gas systems with abundant gas seeps, pockmarks, and shallow gas fronts (e.g. Polikarpov et al., 1989; Egorov et al., 1998, 2011; Artemov et al., 2007; Naudts et al., 2008; Nikolovska et al., 2008; Greinert et al., 2010; Diaconu et al., 2020; Römer et al., 2020)..

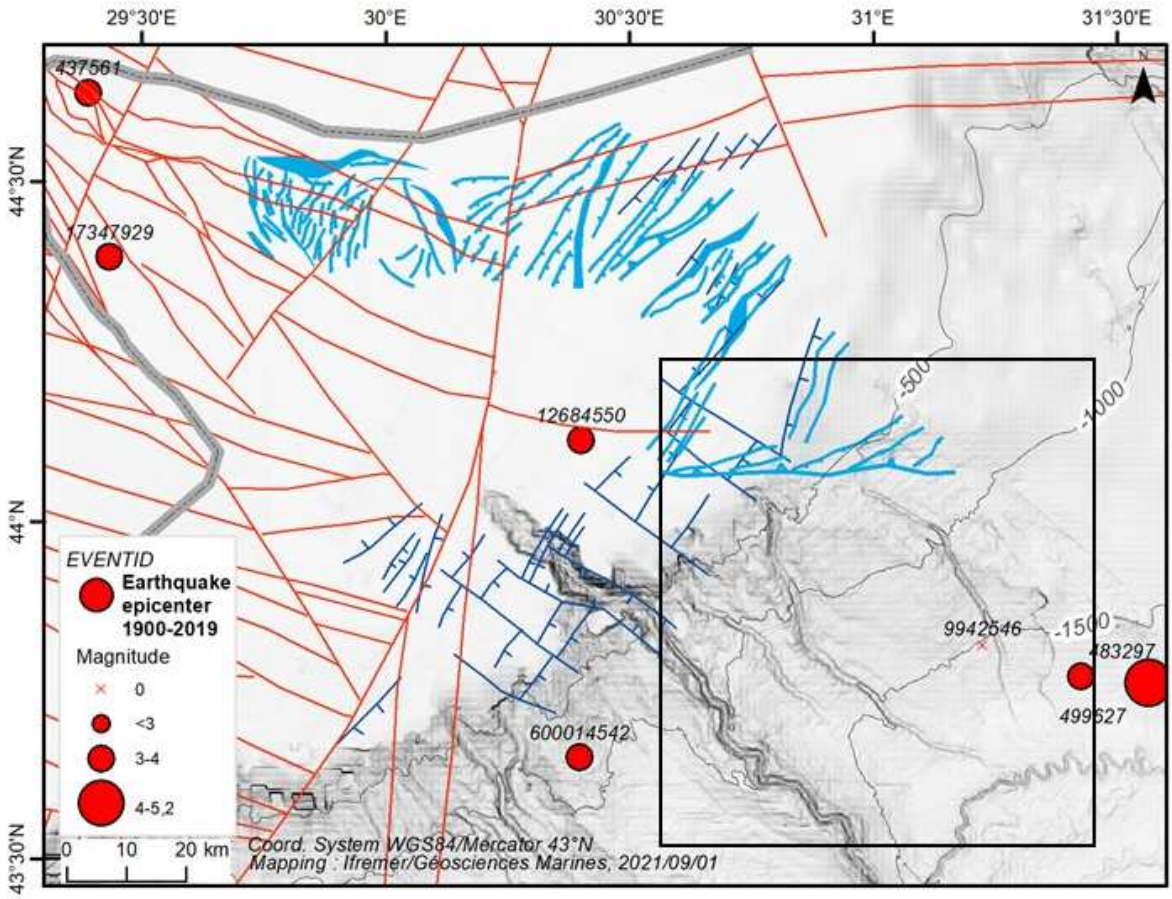

Fig. 2. Morpho-bathymetric map based on EMODNET2016 and GEBCO2014 bathymetric data with superposed structural map, offshore Romania. Note the distribution of canyons and paleo-valleys. The distribution of faults is indicated with: in red, compilation from Diaconu et al., 2020 from the data of Dinu et al., 2005; Morosanu, 2007 and Munteanu et al., 2011; in light blue, gravitational faults from Tambrea et al., 2002 and Dinu et al., 2003; in dark blue gravitational faults from Konerding et al., 2010. Note that the sets of faults of different colors have been mapped from distinct and incomplete grids of seismic profiles thus leading to an incomplete map. In grey dotted line, the border of the Histria Basin (from Pătruț et al., 1984 and Anton et al., 2019). The earthquake epicenters (time period 1900-2019) are from the ISC catalog (http://www.isc.ac.uk/iscbulletin/search/catalogue/). The nearest earthquakes of the study area are presented in Table 1. The study area is indicated by the black box (see Fig. 3).

Event	Lat	Long	Mag	Depth (km)	Origin Time	Station	Distance (° and km)
499627	43.7622	31.5640	4.6	37.5	03/03/1986 07:26:08.21	Sevastopol	1.71° ~189 km
12684550	44.1208	30.4006	3.9	10	20/06/2007 22:34:07.33	Tirgusor	1.47° ~163 km
12701122	43.9301	31.6372	4	3.7	18/02/2009 09:44:10.49	Sevastopol	1.58° ~175 km
600014542	43.6516	30.3969	3.1	12	25/08/2011 08:22:40.42	Mangalia	1.32° ~146 km

Table 1: Earthquake Data extracted from the International Seismological Centre (2020). Errors are not reported in the catalog. Distance in km from the closest station was calculated with 1° = ~ 111 km.

2.2 Previous work on the study area

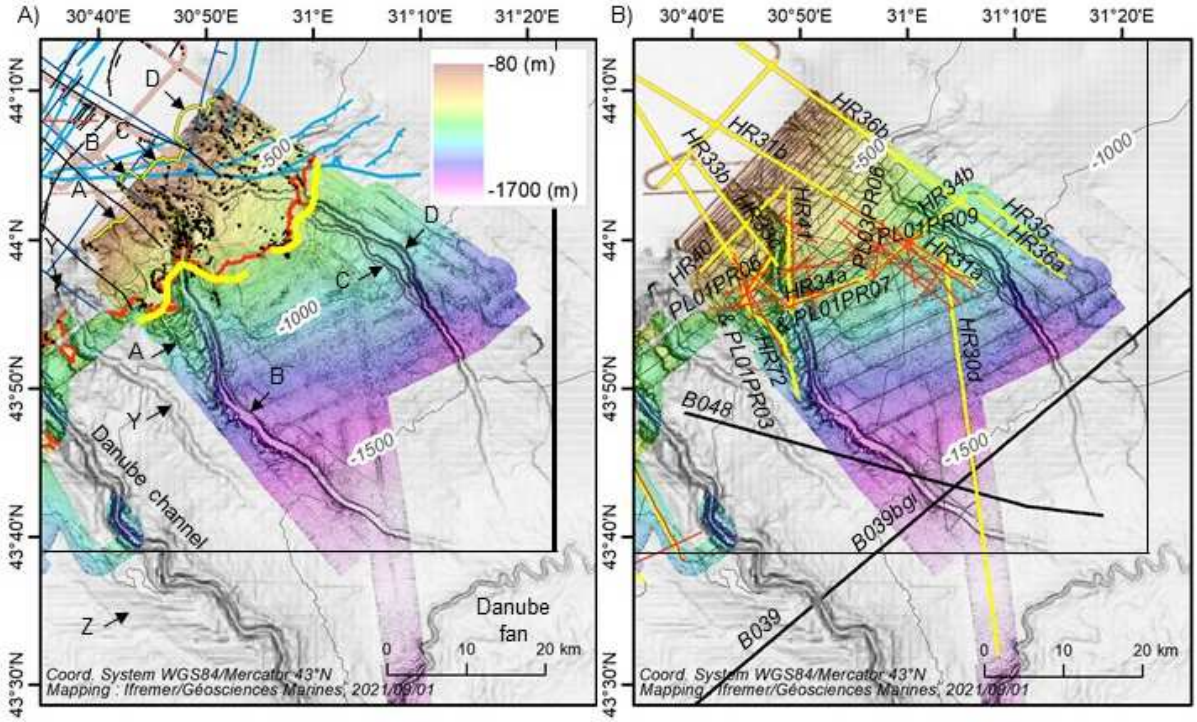

Fig. 3. Presentation of the study area (see location on Fig. 2). A) Geological setting showing the shelf break (dark yellow line) (Riboulot et al., 2017), the canyons/paleo-valleys and associated channel complexes (A, B, C, D, Y and Z), the Danube channel and Fan, the morphology lines i.e. sedimentary ridges (black barbed wires) (Assemblage project), the faulting pattern (see Fig. 2 for references), the upper limit of the model-predicted steady-state GHSZ (red line) (from Ker et al., 2019) and the observed BSR (yellow line) (Colin et al., 2020b) and, the gas flares (black dots, Riboulot et al., 2017). B. Location of seismic data acquired during GHASS and Blason surveys showing high-resolution seismic profiles (yellow lines, 2015 GHASS cruise; bold black lines, 1998 Blason cruise DOI 10.17600/98020030), SYSIF profiles (red lines), sub-bottom profiles (black lines, 2015 GHASS cruise, DOI 10.17600/15000500). Basemap: Morpho-Bathymetric map based on EMODNET2016 and GEBCO2014 bathymetric data (grey map) with superposed bathymetry from GHASS (2015) (colored map). The black box corresponds to the maps presented in Fig. 7, 15, 19, 20.

The study area lies to the northeast of the Danube paleo-delta basinward of the shelf-break from around 180 to 1300 m water depth (Fig. 3A). The continental slope varies around 2°-4°

between 200 and 500 m water depth respectively and up to 35° locally (canyon side walls). The outer shelf and upper slope are incised by several canyons formed by erosion prolonged on the middle and lower slope to channel-levees (e.g., Popescu et al., 2002; Riboulot et al., 2017). Around 20% of the seafloor surface is disturbed by scarps linked to instabilities. The scarps mainly occur in the canyons and paleo-valleys. Scarps also occur on the open upper slope between 200 and 500 m water depth. MTDs have been observed between 200 and 900 m water depth (Riboulot et al., 2017; Hillman et al., 2018). Seaward of the study area, the deep-sea thick deposits of mostly clayey sediments were mainly supplied by the Danube and the Dnepr Rivers (Soulet et al., 2013; Matenco et al., 2016). Faults of interest in our study area are faults related to the Messinian gravitational collapse and younger reactivations mainly during middle Pliocene (Dacian, in local stage) (Tambrea, et al., 2002; Dinu et al., 2003; Munteanu et al., 2012; Schleder et al., 2016). The first generation (Middle Pontian) gravitational faults are related to the so-called “eastern gravity-driven deformation system” of Schleder et al. (2016) characterized by an updip extensional domain with SW-NE oriented normal faults partially accommodated by a downdip contractional domain marked by a mainly W-E oriented thrust (Tambrea, et al., 2002; Dinu et al., 2003; Munteanu et al., 2012; Schleder et al., 2016) (in light blue on Fig. 2, Fig. 3A and, Fig. 19B). Second generation (Dacian) gravitational faults have been observed in a grid of seismic profiles located near the shelf edge. These faults form mostly NE-SW trending grabens and horsts separated by NW-SE oriented transfer faults (Bega and Ionescu, 2009; Konerding et al., 2010) (in dark blue on Fig. 2, Fig. 3A and Fig. 19B).

The presence of gas hydrates is inferred from the identification of the Bottom Simulating Reflector (BSR), which marks the base of the Gas Hydrate Stability Zone (GHSZ). The GHSZ corresponds to the zone where gas hydrates (Sloan, 1990, 1998; Kvenvolden, 1993), i.e. the ice-like solid form of gas, develop under conditions of low temperature, high pressure, and sufficient gas concentrations (Kvenvolden and McMenanim, 1980; Sloan, 1990, 1998; Dickens and Quinby-Hunt, 1997). The BSR was first mapped by Ion et al. (2001), then Popescu et al. (2006). Pockmarks, gas flares, and seismic facies related to the presence of

gas have been also reported. The gas flares were generally acoustically detected in the water column upward the landward limit of the GHSZ at 660 m water depth (Popescu et al., 2004; Riboulot et al., 2017). They mainly consist of gas emissions released to the ocean from the seafloor from underlying sources. Finally, the study area has undergone major changes in environmental conditions relative to sea-level changes and induced connection-disconnection of the Marmara-Mediterranean Sea during last interglacial-glacial cycles (Soulet et al., 2011; Constantinescu et al., 2015; Wegwerth et al., 2015; Ballas et al., 2018). These cycles cause alternating marine and freshwater lake conditions (Badertscher et al., 2011) and connection-disconnection between the Danube River, its canyon, and consequently the deep-sea deposit systems (Lericolais et al., 2009; Constantinescu et al., 2015).

3. Methodology

The results presented in this paper originate from the interpretation of several data sets including (Fig. 3B):

(1) Multi-beam echo-sounder data acquired during the GHASS (2015) campaign (Reson SeaBat 7111 for shallow water 5-500 m, and 7150 for deeper water 200-2000 m) with a bathymetric resolution of 20 m (already published). They have provided the geomorphology of the seafloor from a dense grid of profiles. Water column acoustic data processed on board with SonarScope and GLOBE software have provided the distribution of gas flares. These profiles have not been mapped on Fig. 3B.

(2) 2D-high and very-high-resolution (VHR) seismic reflection profiles acquired during the 1998 BlaSON surveys of Ifremer and GeoEcoMar. High-resolution seismic profiling was implemented using a mini-GI air-gun seismic source (frequency range 150 Hz and vertical resolution of 2.5 m) and a 24-channel streamer. Sub-bottom profiles (Chirp) were acquired simultaneously to investigate surficial sediments.

(3) 2D-high-resolution (HR) multi-channel seismic profiles acquired during the GHASS survey using a single 24/24 mini-GI air-gun seismic source (central frequency at 115 Hz and vertical resolution of 3.2 m) for profiles GAS031, GAS033 to GAS039, two 24/24 for profile GAS030, a single 13/13 for profiles GAS040 and GAS041, and a 96-channel solid streamer (inter-trace of 6.25 m and maximum source-receiver offset of 650 m). These profiles are named HRxxx in Fig. 3B. The seismic dataset was processed using a conventional post-stack sequence with constant velocity (1500m/s) (Ker et al., 2015).

(4) 2D-very high-resolution hull-mounted Sub-Bottom Profiler (SBP) data acquired during the GHASS survey. The SBP operates at the frequency range 1800-5300 Hz, giving a vertical resolution close to 20 cm. The quality control of SBP data was performed using the Ifremer QC Subop software (Dupont, 2015; Ker et al., 2015).

(5) 2D-very high-resolution deep-towed seismic profiles were acquired with the Ifremer SYSIF system (Marsset et al., 2010; Marsset et al., 2014; Marsset et al., 2018) during the GHASS survey. SYSIF is a deep-towed seismic device hosting a Janus-Helmholtz transducer emitting a linear chirp signal in the frequency bandwidth 220-1050 Hz and a streamer, both towed at 2 knots, 100 meters above the seafloor. Processing includes correction of altitude, and seismic signature deconvolution and provides 15-m-lateral resolution at the seafloor and 1-m-vertical resolution.

All seismic data were integrated into IHS Kingdom software for interpretation. Measurements in meters were calculated from Two-Way Traveltime (TWT) values using v= 1500 m/s.

Seismic interpretation is based on: (1) analysis of the reflectors' lateral terminations (onlap, down lap, erosional truncation) according to the general principles of seismic stratigraphy (Mitchum et al., 1977); and (2) characterization of seismic facies and correlation of distinctive reflectors between profiles. The cross-correlation between complementary seismic datasets provided mapping of unconformities, sedimentary bodies, faults, and gas systems. SBP profiles are not presented in this paper due to the poor quality of data caused by the presence of shallow gas. Only one Blason profile is presented. SYSIF was mainly used to identify sedimentary discontinuities such as scarps related to MTDs, channel sidewalls, and

faults. It also allowed to identify facies and seismic anomalies related to fluid/gas features and consequently permeable and seal layers. All seismic profiles are presented with overlapped interpretative line drawing in this paper.

4. Results

4.1 Seismic units and facies.

Architecture of the study area consists of the stacking of different types of seismic units classically encountered in similar slope and turbidite environments (e.g. Twichell et al., 1991; Piper et al., 1997; Droz et al., 2003; Madof et al., 2009) and already identified in the Danube Fan (Zander et al., 2017; Hillman et al., 2018; Winguth et al., 2000; Popescu et al., 2004;). The majority of these units are the channel/levee systems and MTDs. For the remaining units, deposits correspond to infilling and draping near seafloor units. A detailed description of these units and their relationship with faults, gas signatures and key surfaces, in terms of sequential stratigraphy, is proposed in sections 4.2 to 4.6.

Mass Transport Deposits

MTDs are of two types and two generations, either 1) irregular masses of wide lateral extent (up to 300 km^2 in size and up to 80 m in thickness) characterized by a transparent to chaotic high amplitude facies, a very irregular top surface with hyperbolic reflections and an erosive basal surface, truncating underlying reflections. These MTDs are localized over a basal major erosional surface (e.g. MTD12 in Fig. 4); or 2) small masses up to around 10 km^2 in size and 35 m thickness characterized by hummocky, transparent to chaotic, and irregular seismic facies, with continuous, low to high amplitude reflections and an erosive basal

surface. These MTDs are near the seafloor, localized at the upper slope and channel walls, where they rework superficial deposits (e.g. MTD2 in Fig. 8B).

Channel-levee systems

The channel is generally V-shaped with an erosional base. The levees are wedge-shaped and characterized by low amplitude, high frequency, remarkable continuity of reflectors. The lateral extent and thickness of channel-levees are variable. Some channels form a channel complex (e.g. channel complex B in Fig. 8A).

Filling sedimentation

The channel-levees abandonment is marked by channel infilling with transparent facies interpreted as distal overbank deposits from younger channels (e.g. Filling unit in Fig. 8A).

Draping sedimentation

The study area is covered by a draping unit of low amplitude, low frequency and continuous parallel reflectors interpreted as very fine-grained sediments. The thickness of this unit ranges from 20 to 40 m (e.g. Draping unit in Fig. 8A).

4.2 Basal regional unconformity, slide scarps, and associated MTDs

A basal and regional unconformity, ranging between 300 m below the seafloor (mbsf) upstream to locally 10 mbsf downstream, has been identified despite the scarcity of HR seismic profiles (Fig. 4A). This unconformity corresponds to an erosional surface that truncates reflections of underlying seismic units (Fig. 4C). It is generally well expressed in the middle slope but poorly visible in the upper slope due to the presence of gas (Fig. 4B), except in the western part of the study area (see section 4.3).

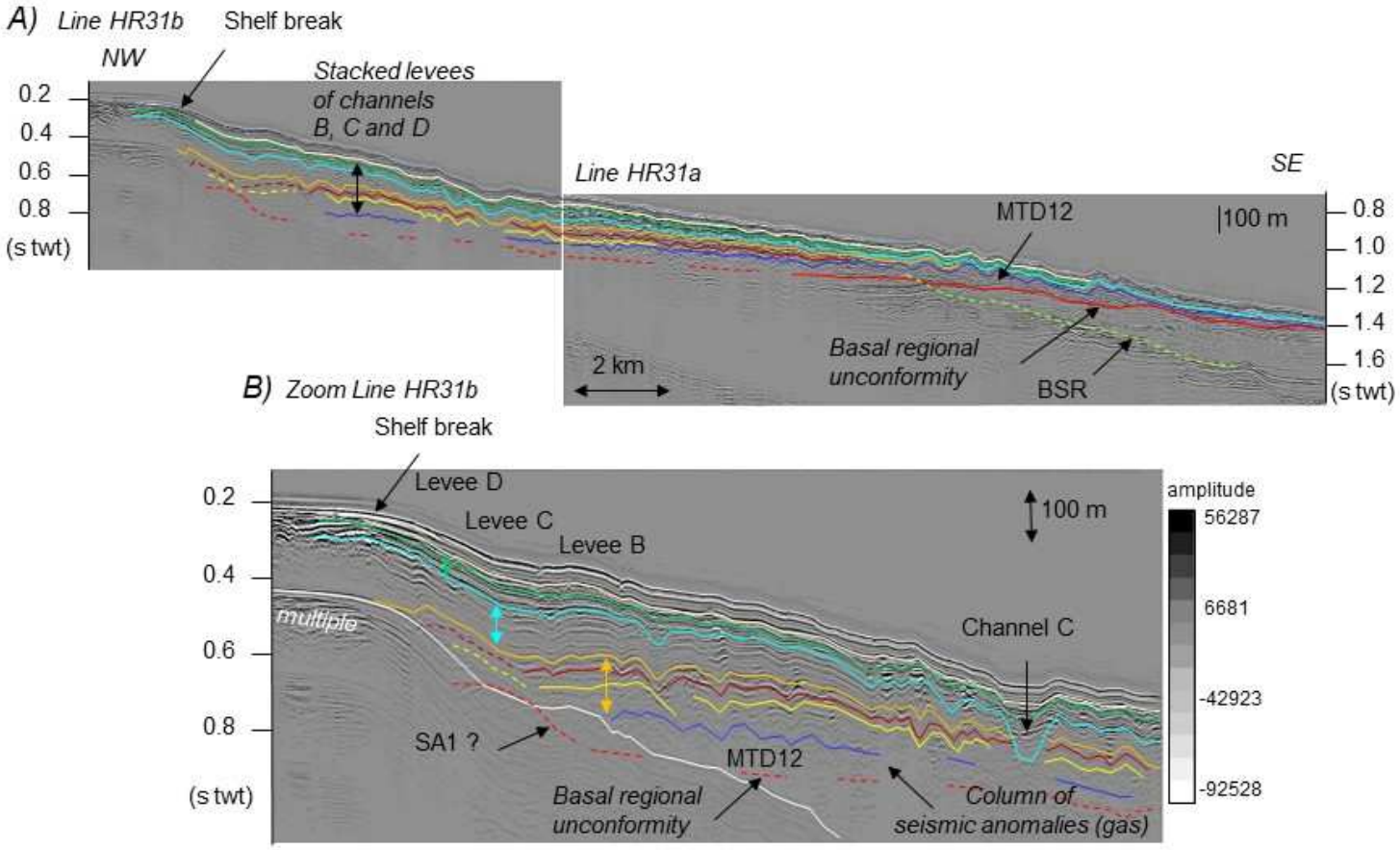
A) Line HR31b
Shelf break
NW
Stacked levees
of channels
B, C and D
0.2
0.4
0.6
0.8
(s twt)
Line HR31a
SE
MTD12
100 m
0.8
1.0
1.2
1.4
1.6
(s twt)
2 km
Basal regional
unconformity
BSR
B) Zoom Line HR31b
Shelf break
Levee D
Levee C
Levee B
100 m
amplitude
56287
6681
-42923
-92528
multiple
Channel C
SA1 ?
MTD12
Basal regional
unconformity
Column of
seismic anomalies (gas)

326

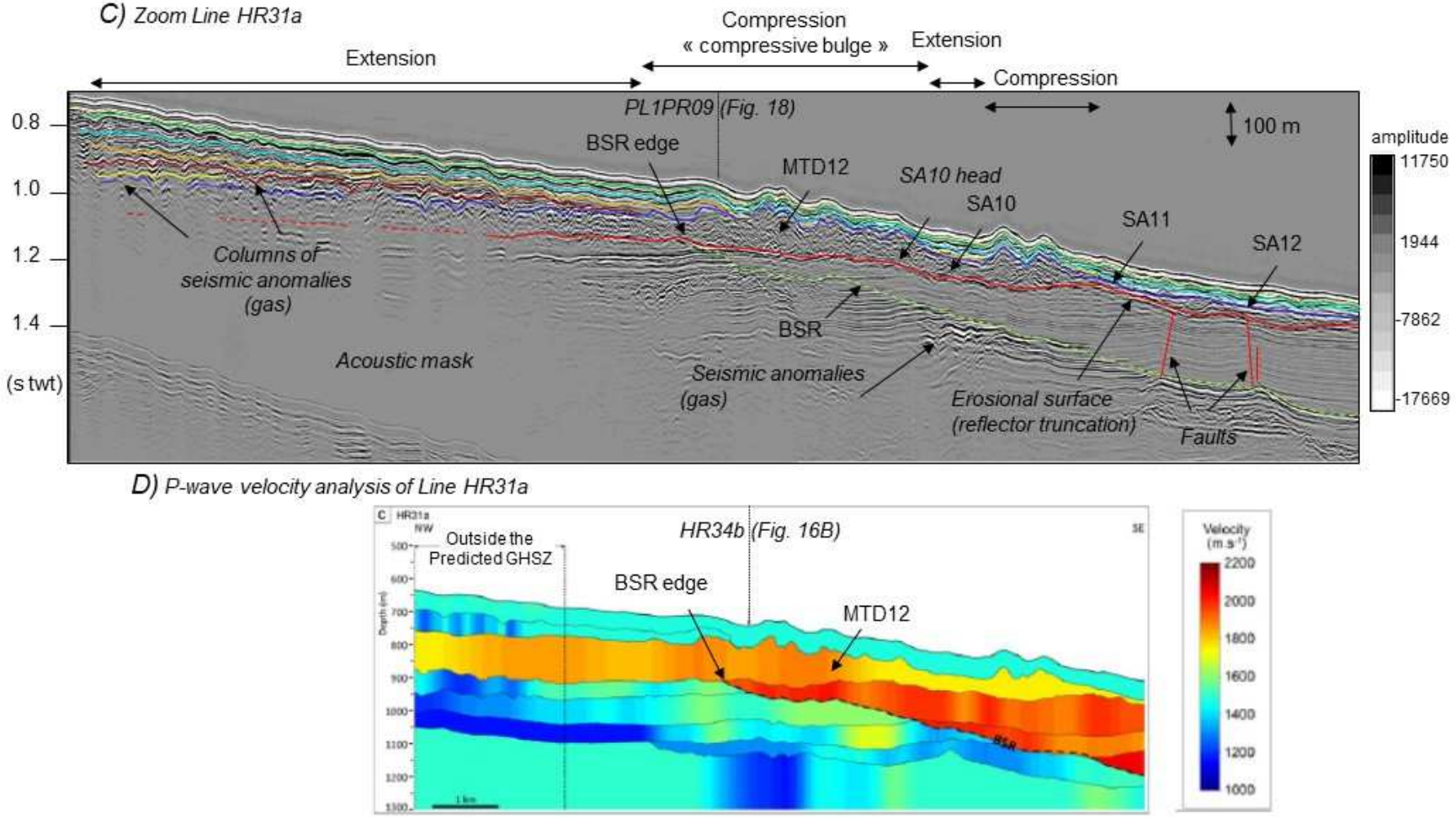
C) Zoom Line HR31a
Extension
Compression
« compressive bulge »
Extension
Compression
PL1PR09 (Fig. 18)
100 m
amplitude
11750
1944
-7862
-17669
0.8
1.0
1.2
1.4
(s twt)
BSR edge
MTD12
SA10 head
SA10
SA11
SA12
Columns of seismic anomalies (gas)
BSR
Acoustic mask
Seismic anomalies (gas)
Erosional surface (reflector truncation)
Faults
D) P-wave velocity analysis of Line HR31a
HR34b (Fig. 16B)
Outside the Predicted GHSZ
BSR edge
MTD12
BSR
Velocity (m.s-1)
2200
2000
1800
1600
1400
1200
1000

327

Fig.4. Seismic characteristics of the basal regional unconformity, scarp alignments (SA), MTDs, BSR and gas/GH. A) The high-resolution seismic dip Line HR31a-b (for location see Fig. 3B) shows the extent of the basal unconformity. B) Zoom of Line HR31b showing the shelf break and SA1 (see Fig. 7). The upstream part of the basal unconformity and SA1 are not very clear due to the presence of gas. Note the location of MTD12 over the unconformity. The upper colored reflectors correspond respectively to the top of the levees of channel complex B (yellow, brown, orange), channels C (turquoise blue) and D (green) and upper units (light yellow and seafloor). The crossing of the Line with channel C is indicated (Fig. 3B). C) Zoom of Line HR31a showing the lower part of the basal regional unconformity. Note: the truncation of reflectors of underlying layers of this unconformity interpreted as an erosional surface; the presence of SA10 to SA12 on the erosional surface (see Fig. 78); the extensive part (low deformation) of MTD12 downstream SA10 (Fig. 4C) and the compressive part (high deformation) just upstream SA11; the chaotic facies of MTD12 and the hummocky top surface of the compressive bulge; the BSR (light green color) and seismic anomalies related to gas beneath; the acoustic mask and columns of seismic anomalies upstream the BSR edge. D) P-wave velocity analysis of Line HR31a. Note the velocity range (1900-2050 m/s) which characterize the GH just above the BSR and the velocity range within MTD12 (1750-1900 m/s). The low velocity values (1200-1500 m/s) indicate the presence of free gas-bearing sediments (from Ker at al., 2019).

This erosional surface is characterized by several scarps (Fig. 4C; Fig. 5). The scarps were manually picked and mapped and vary in dimension, i.e. length (L) and height (H). Scarp alignments called SA (SA1 to SA13) have been identified (see for example Fig. 5 and Fig. 6) partly based on their dimensions and/or dip changes of underlying reflectors and their mapping shows a general NE-SW orientation (Fig. 7A). Dip changes in stratifications are characteristic of this area and are discussed in section 5.1. The basal unconformity displays two major erosional troughs up to around 300 m below paleo-valleys A and B (see the detailed description of paleo-valleys in section 4.3) (Fig. 8A). These erosional troughs are

356 characterized by a notably irregular topography due to numerous scarps along the dip
357 profiles, particularly for paleo-valley A (Fig. 9).
358

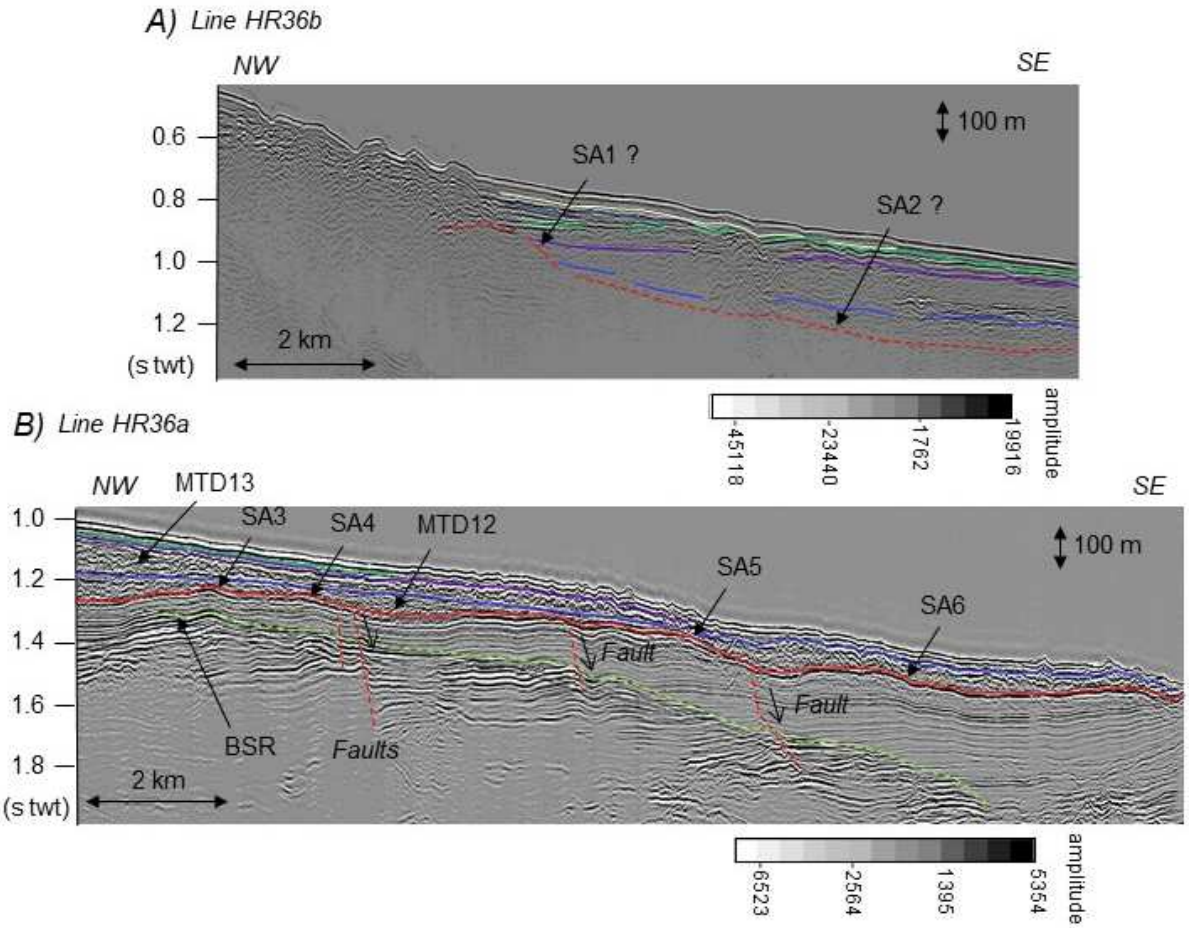

359
360 *Fig. 5. Example of normal faults below scarp alignments in the eastern part of the study area.*
361 *A) The high-resolution seismic Line HR36b (for location see Fig. 3B) shows the shelf break,*
362 *SA1 and SA2 (see Fig. 7) and overlying MTD12 and MTD13. B) Line HR36a showing SA3 to*
363 *SA6 and normal faults below these scarp alignments within the GHSZ. Note the listric shape*
364 *below SA5. Arrows to the hanging wall/foot wall define the sense of motion.*
365
366

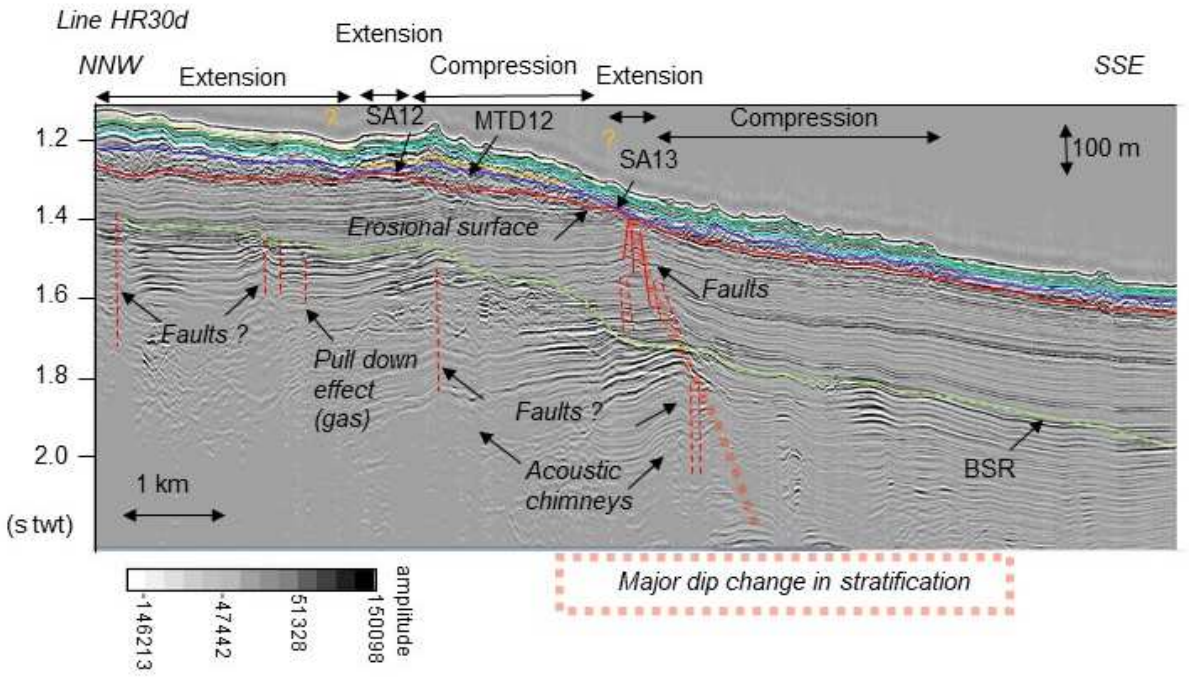

Fig. 6. Relationship between scarp alignments of the erosional surface, MTDs, BSR, and faults. The high-resolution seismic Line HR30d (for location see Fig. 3B) shows the stacked small-offsets of reflectors (faults?) and pull down effects (gas?) below the BSR (in light green). Note the faults and the major dip change in stratification below SA13 at the erosional surface and the accordion-like shape of MTD12 with alternating extensive and compressive parts. Note at SA12, the location of the head of the extensive part which is generally the case on profiles.

375

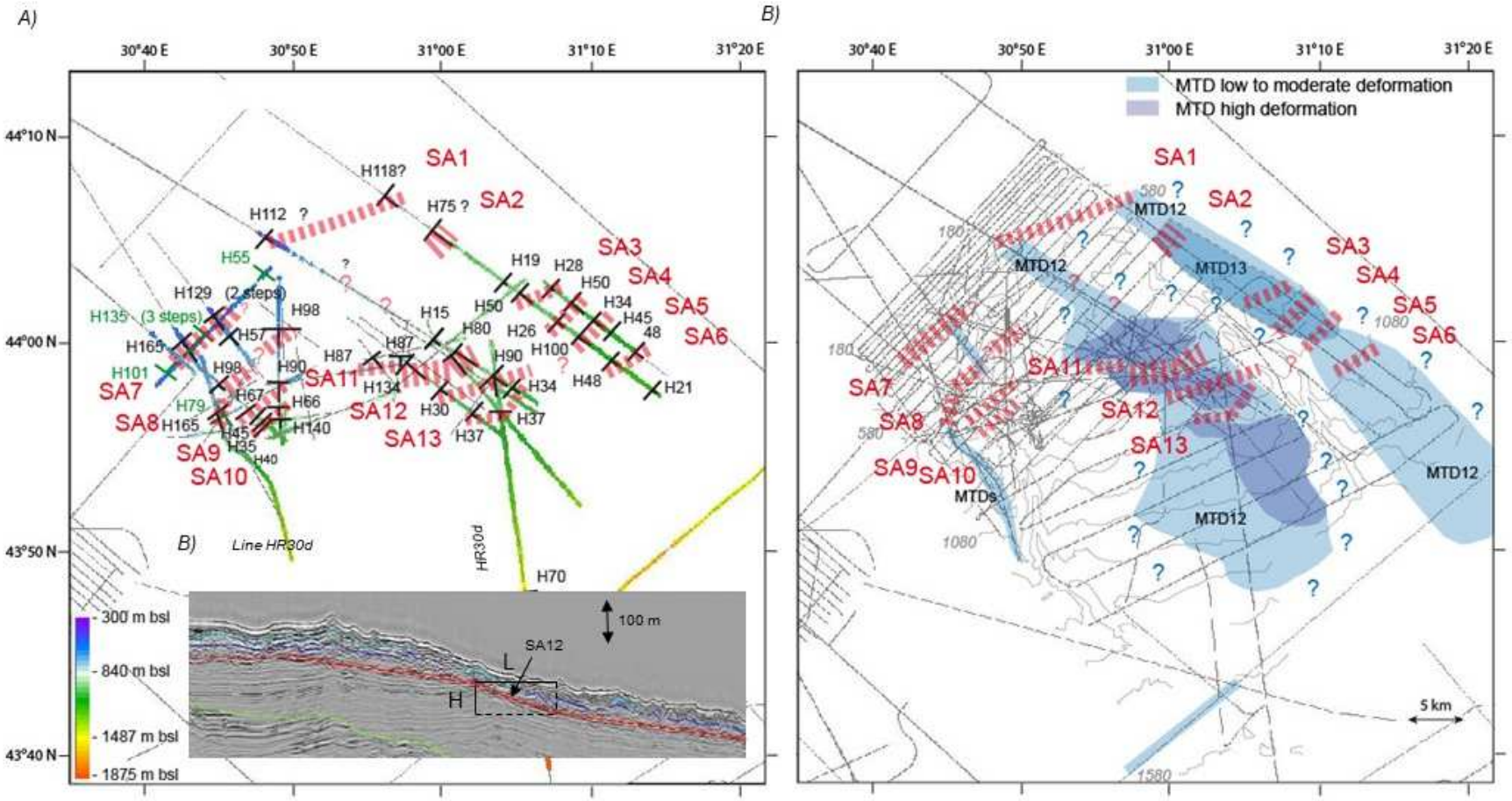
A)
B)
30°40 E
30°50 E
31°00 E
31°10 E
31°20 E
44°10 N
44°00 N
43°50 N
43°40 N
SA1
SA2
SA3
SA4
SA5
SA6
SA7
SA8
SA9
SA10
SA11
SA12
SA13
H118?
H112 ?
H75 ?
H55
H129 (2 steps)
H135 (3 steps)
H165
H101
H98
H57
H67
H66
H79
H140
H45
H35
H40
H87
H15
H80
H26
H19
H28
H50
H34
H45
48
H100
H90
H134
H30
H37
H48
H21
H70
B) Line HR30d
HR30d
300 m bsl
840 m bsl
1487 m bsl
1875 m bsl
100 m
SA12
L
H
MTD low to moderate deformation
MTD high deformation
MTD12
MTD13
MTDs
180
580
1080
1580
5 km

376

Fig. 7. Map of the basal regional unconformity and associated MTDs (see location on Fig. 3). A) Map showing the seismic-bathymetry of the basal erosional surface and the scarps from HR and SYSIF seismic profiles. The dash in black crossing the profile corresponds to a scarp, the value in meter (Hxx) indicates the scarp height and the length of the dash in black along the profile indicates the horizontal kilometer length of the scarp. The scarps bounding the paleo-valleys A and B laterally are in green to better distinguish these scarps in this area where scarps are numerous. Scarp Alignments (SA) SA1 to SA13 are indicated by dashed red lines. B) Definition of the height and length of the scarp on the seismic profile. C) Map of MTDs covering the basal regional unconformity. This map is based on all seismic data and presents the distribution of MTDs. Scarp alignments SA1 to SA13 have been reported. Note the correlation between the heads of MTD12 and SA1, the location of MTD13 over MTD12 and, the distribution of low (in light blue) to moderate and high deformation (in dark blue) parts for MTD12 with respect to SA1 to SA13. Basemap: morpho-bathymetric map based on EMODNET2016 and GEBCO2014 bathymetric data.

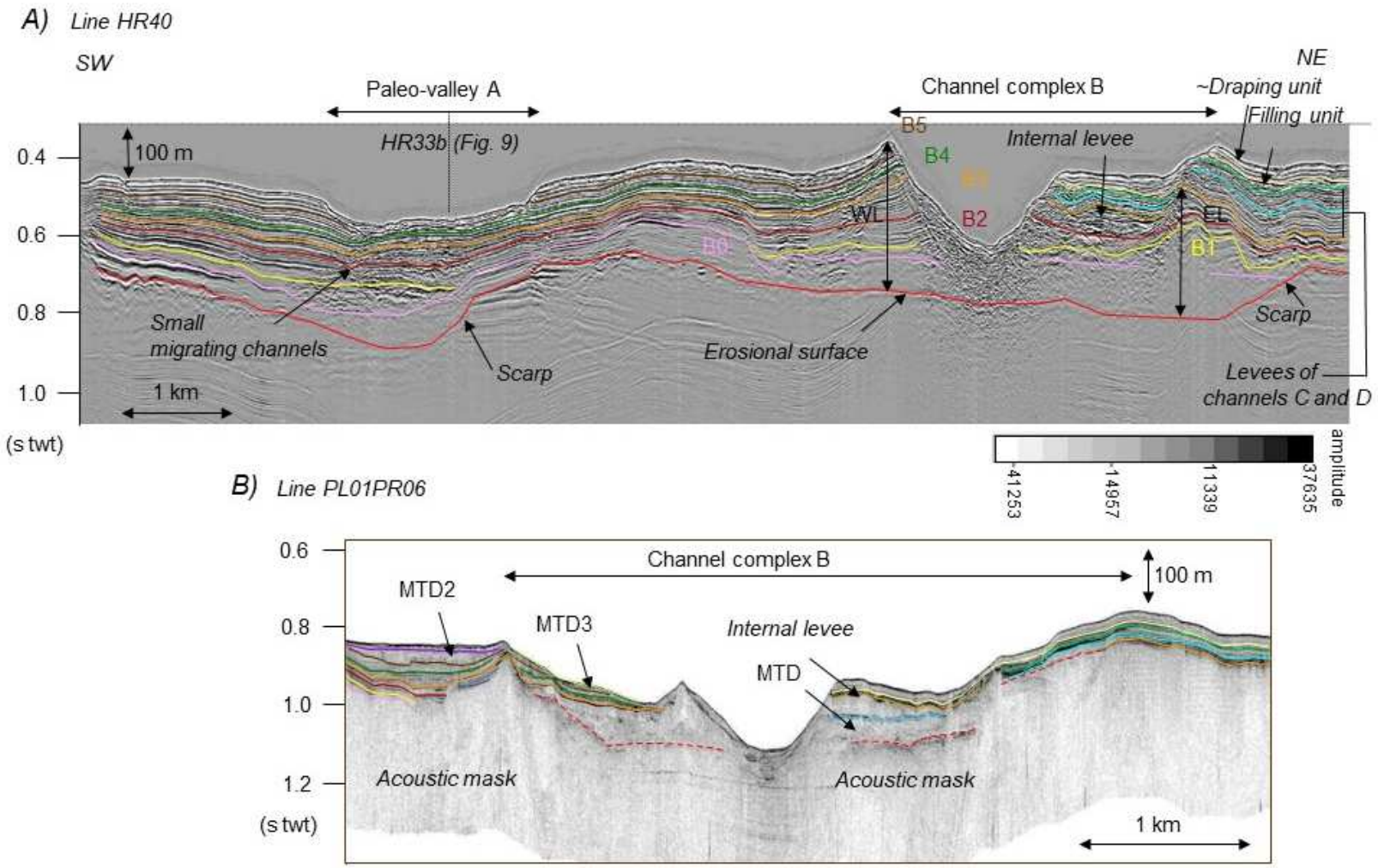
A) Line HR40
SW
NE
Paleo-valley A
HR33b (Fig. 9)
Channel complex B
~Draping unit
Filling unit
Internal levee
100 m
B5
B4
B3
B2
B1
B0
WL
EL
0.4
0.6
0.8
1.0
(s twt)
1 km
Small migrating channels
Scarp
Erosional surface
Scarp
Levees of channels C and D
amplitude
41253
14957
11339
37635
B) Line PL01PR06
Channel complex B
100 m
MTD2
MTD3
Internal levee
MTD
0.6
0.8
1.0
1.2
(s twt)
Acoustic mask
Acoustic mask
1 km

393

Fig. 8. Cross profile of Paleo-valley A and channel complex B. A) The high-resolution seismic Line HR40 (for location see Fig. 3B) shows the cross-section of Paleo-valley A and channels B0 to B5 and the basal erosional surface below. Note: the erosional trough and the lateral scarps marking the base of paleo-valley A and its filling by the western levees of channels of B0 to B5; the stacked migrating small channels within this filling. The channel complex B is marked by an asymmetric shape with a staircase structure of the eastern side. Note the migration of channels B0 to B2. The double arrows indicate the channels axes of B0 and B1. On the eastern side of channel complex B, the internal levee is considered as coeval to the levees B4 and B5 of the western side. Note the presence of distal levees of channels C and D and the filling and draping upper units. B) The SYSIF PL01PR06 profile (for location see Fig. 3B) shows an example of superficial MTDs i.e. MTD2 and MTD3 within paleo-valley A over the western levee of channel complex B.

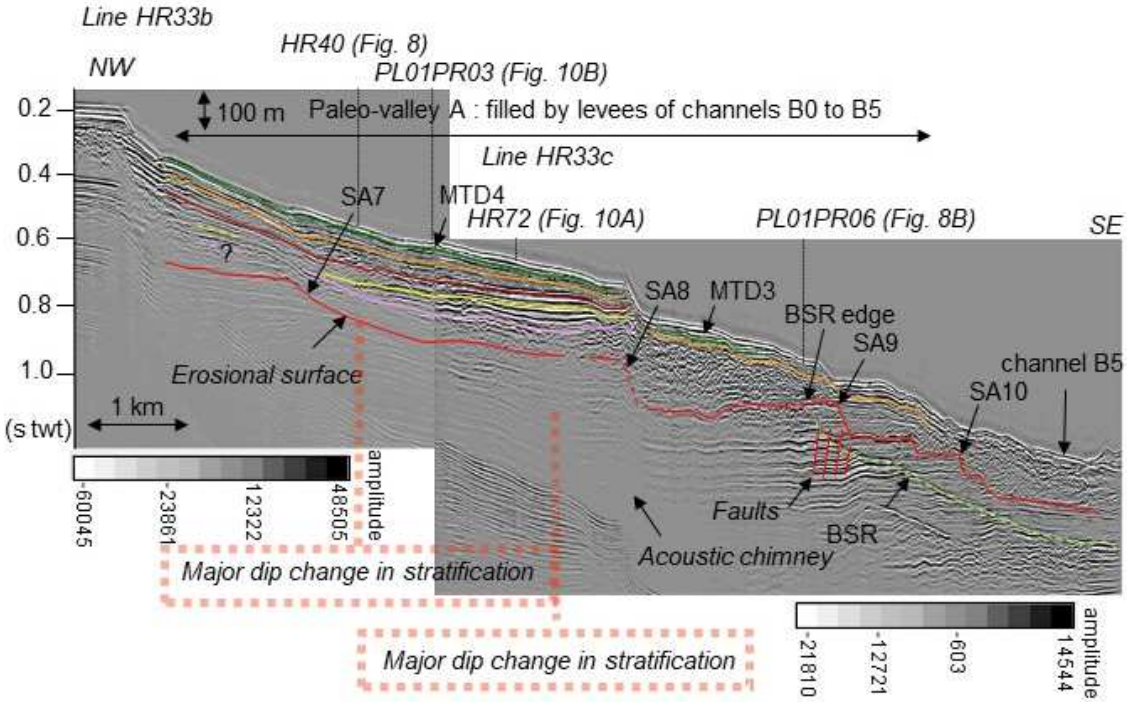

Fig. 9. Dip profile of Paleo-valley A and channel complex B. The high-resolution seismic Lines HR33b and HR33c (for location see Fig. 3B) show the cascading scarp alignments SA7 to SA10. Note the location of MTD4 and MTD3 near the sea floor and over respectively

411 *intervals SA7-SA8 and SA8-SA9; the set of high-angle parallel faults showing small offset at*
412 *the BSR edge and below SA9.*
413
414 Wide MTDs lie directly over the erosional surface below the slope (see MTD12 on Fig. 4A
415 and Fig. 4C) and at the bottom of paleo-valleys A and B (see section 4.3, Fig. 10; Fig. 16).
416 The map of MTDs associated with the erosional surface show two MTDs of wide extent i.e.
417 MTD12 and MTD13 (over MTD12) of at least respectively 300 and 75 km^2 in size and
418 between 10 to 80 m in thickness (total volume > 50 km^3) (Fig. 5 and Fig. 7B). The upstream
419 limit of MTD12 correlates with scarp alignments (SAs) SA1 and SA7 (Fig. 7B). MTD12
420 extends over several SAs basinward. It is characterized by an accordion-like external shape
421 with generally upper extensive parts at the scarp heads and compressive bulges several
422 kilometers from the scarp heads (Fig. 4C; Fig. 6). This implies that the SAs correspond to
423 slide scars and that a polyphase slide event disturbed the slope deposits.
424 We underline the presence of a deeper (older) erosional surface covered by MTDs (see
425 section 4.3, Fig. 13A, erosional surface 2). This surface is cut by the basal regional surface
426 described above and the erosive axis of paleo-valley B. No further description is possible as
427 only a few seismic lines were available to image such deep structures.
428

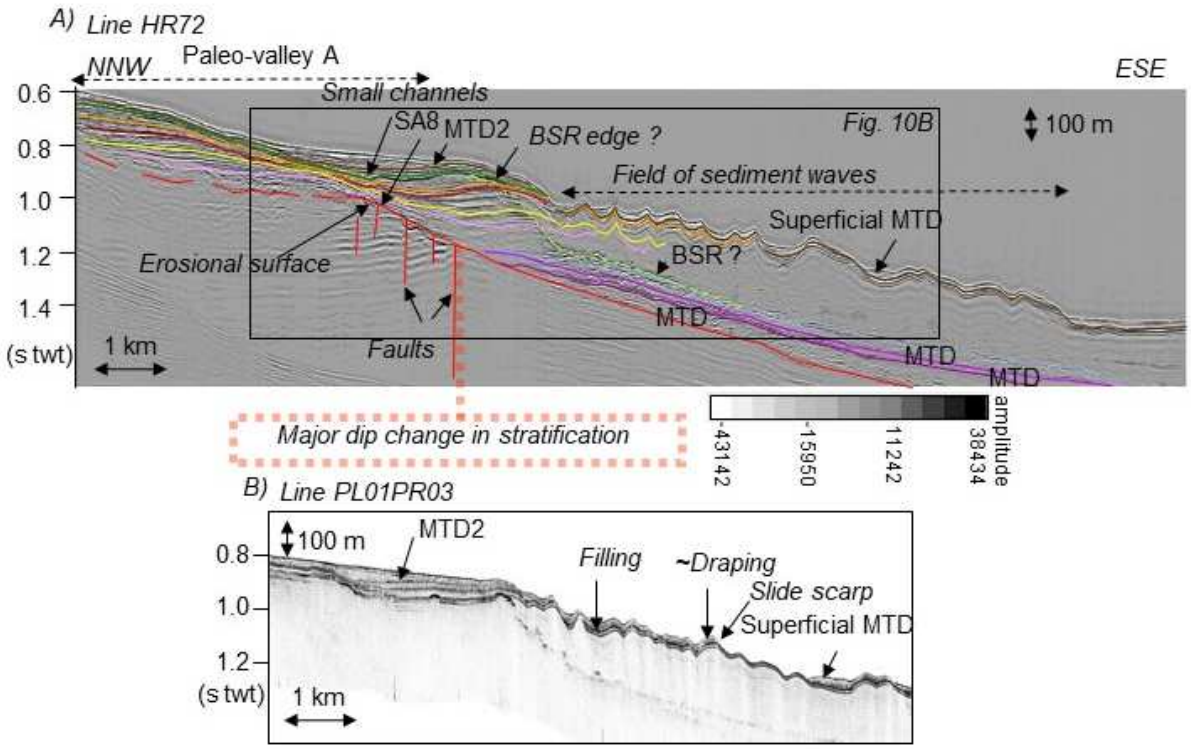

Fig. 10. MTDs and sediment waves field within paleo-valley A. A) The high-resolution seismic Line HR72 (for location see Fig. 3B) shows the MTDs overlying the erosional surface. Note the reworking/deformation of levees deposits of channels B0 to B5. The upstream reworking is characterized by stacked small channels and levees deposits and the downstream reworking corresponds to the sediment waves field. Note also the vertical faults at the BSR edge and below SA8. B) SYSIF profile PL01PR03 showing the sub-surface MTD2 and the superficial MTD associated to the slide scarp within the draping unit at the top of the filling unit.

4.3 Geometry and internal structure of paleo-valleys and channel-levee systems

Five to six main paleo-valleys - A, B, C, D, (Y) and the Danube connected to the Danube (Viteaz) canyon - characterize the region (Fig. 2, Fig. 3). The Danube canyon/valley has already been described by Popescu et al. (2004) as an erosional major trough with steep flanks which incises the shelf at around 200 m water depth. Partial infilling of the canyon

followed this initial erosional phase. The flat bottom of this through corresponds to the bottom of the main valley and is incised by a V-shaped thalweg that continues beyond the shelfbreak as an entrenched thalweg with well-developed lateral levees in the youngest Danube channel (Popescu et al., 2004). For consistency, we refer in this study to this description to define the terms of canyon, valley and channel-levees (see section 4.1 for the detailed description of channels and levees).

The geomorphology of paleo-valleys B and D has already been described by Riboulot et al., (2017). Paleo-valley A is not clearly expressed on the seafloor. Paleo-valley C shows a wide thalweg but its head is not clearly identified. The present seismic analysis has provided the geometry and internal structure of paleo-valleys and associated channel-levee systems, as well as their stacking pattern and the relative chronology as follows:

-Paleo-valley A appears over a U-shaped erosional trough of 1 to 4 km wide and ~150 m (head) to ~90 m (distal part) deep possibly connected to canyon A. As mentioned previously, the base of the trough is shaped by the erosional surface which is characterized by numerous scarps. More specifically, the lateral scarps define the walls (Fig. 8; Fig. 7 scarps in green) of the trough, and the basal cascading scarps SA7 to SA9 characterize the staircase topography of the bottom along the dip profile (Fig. 9). Three main MTDs lie on the bottom of its downstream part (Fig. 10). It is worth noting that valley A is filled by the stacked western levees of channel complex B i.e. B0 to B5. In the valley axis, the deposits of these levees are locally incised by small migrating channels (Fig. 8; Fig. 10). Downstream, over the basal MTDs, the levee deposits are shaped like a field of sediment waves (Fig. 10). A buried channel-levee system is observed off paleo-valley A and could correspond to the distal part of a channel belonging to channel complex A which seems to have disappeared (Fig. 11, channel A).

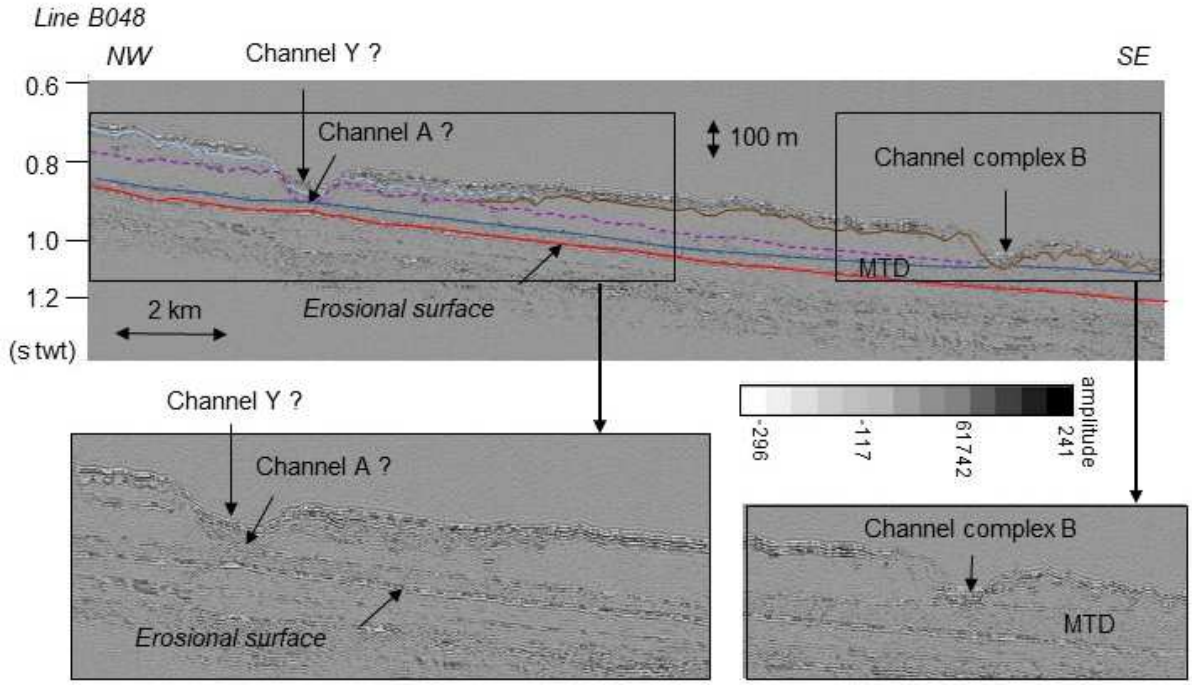

469

470 *Fig. 11. Possible channels A and Y. The high-resolution seismic Line Blason B048 (for*
471 *location see Fig. 3B) shows two superposed channels that could correspond from bottom to*
472 *top to the channels A and Y. Note the stratigraphic location of channel complex B between*
473 *these two channels.*

474

475 -Canyon B (2.2 km wide and ~150 m deep) and its associated paleo-valley B are
476 characterized by an axial thalweg (Fig. 3A) which is connected basinward to the youngest
477 channel-levee system i.e. B5 (channel width of 800 m at ~ 1500 m water depth) of channel
478 complex B (Fig. 8). As mentioned previously, an erosional trough, shaped by the basal
479 unconformity and possibly connected to canyon B appears below this channel complex. (Fig.
480 13A). The singularity of channel complex B is the asymmetry of its walls (Fig. 8 and Fig.
481 13C). Indeed, the western wall is semi-linear whereas the eastern wall presents a staircase
482 structure with two steps. The first channel B0 is located southwest of the present channel
483 then channel B1 migrated northeastward of the present channel (Fig. 8). Channel B2
484 migrated to the position of the present channel. Channel B3 has remained in the B2 position;
485 however, a collapse of its eastern levee has led to the formation of an elongated MTD along

the eastern flank of paleo-valley B (Fig. 12). This explains the complex stair shape of the eastern side of channel complex B (Fig. 13A). An enigmatic mass lies eastward of levee B3 and at the same stratigraphic level. This enigmatic mass shows chaotic seismic facies suggesting deformed sediments but its external shape is regular (Fig. 13A and C). It has been interpreted as belonging to levee B3. It is worth noting that the morphology of the so-called Crest (Riboulot et al., 2017; Ker et al., 2019) results from the topography of levee B3. Channels B4 and B5 have remained in the B3 position and have built their eastern levee directly on the elongated MTD. This has led to the formation of an internal levee in the eastern side of channel complex B. This internal levee reaches a length of 2.5 km and a thickness of 50 m and shows very clear continuous wedging reflections (Fig. 13B, and Fig. 8B).

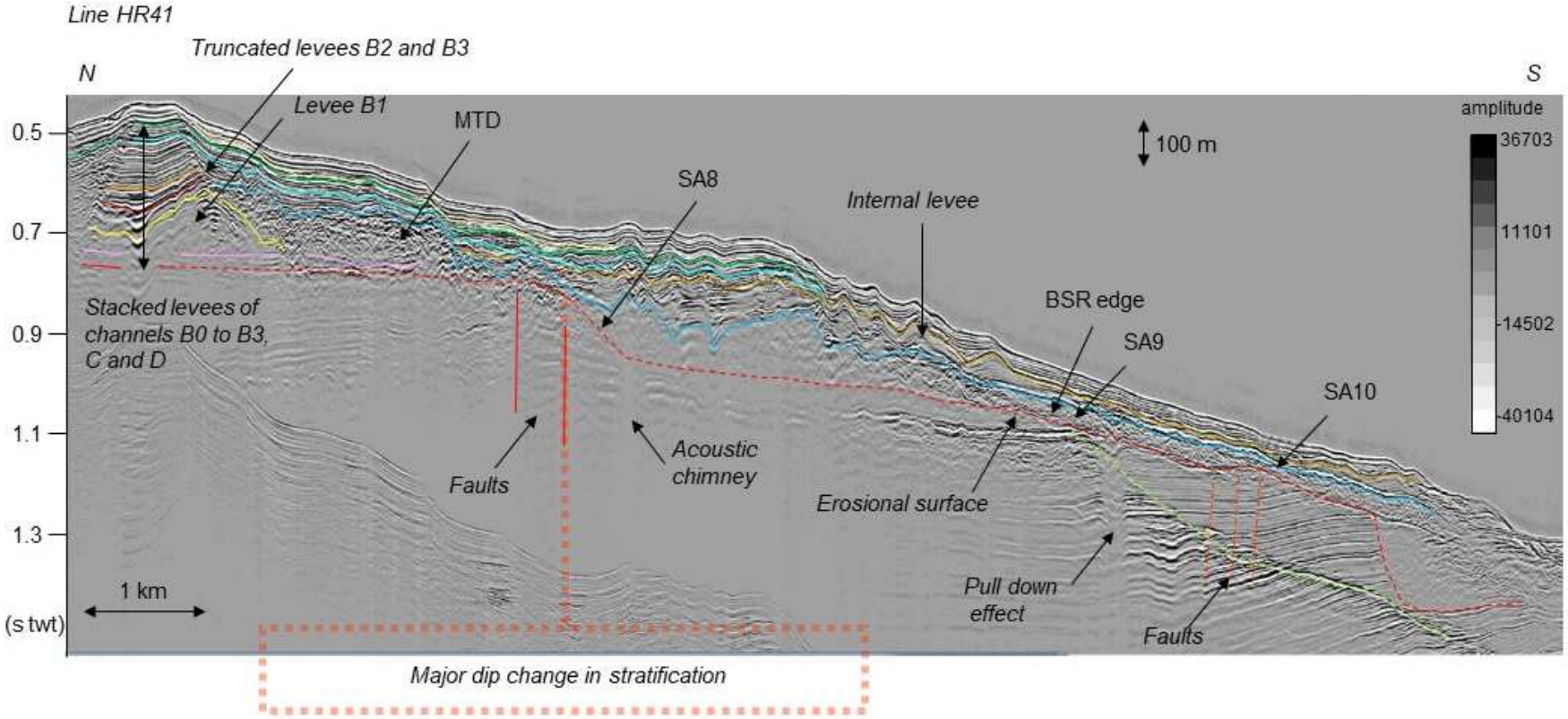

Fig. 12. Dip profile of channel complex B. The high-resolution seismic Line HR41 (for location see Fig. 3B) shows the truncated levees B2 and B3 and the Internal levee coeval to channels B4 and B5 overlying the MTD resulting from the collapse. Basal MTDs on the erosional surface similar to those observed on Line HR72 (see Fig. 10A) are not excluded but the presence of gas does not allow distinguishing these MTDs.

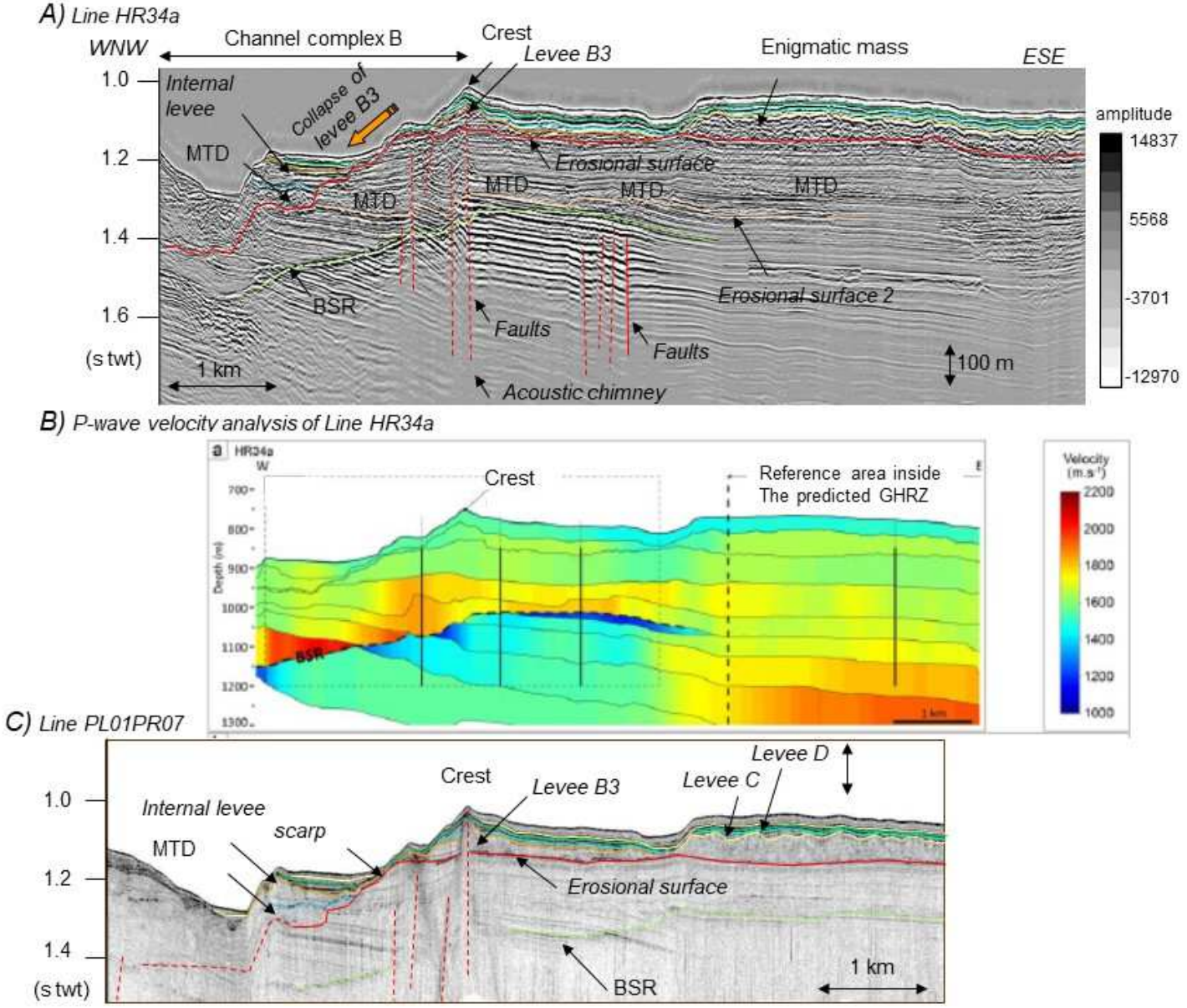
A) Line HR34a
WNW
Channel complex B
Crest
Levee B3
Enigmatic mass
ESE
1.0
1.2
1.4
1.6
(s twt)
Internal levee
Collapse of levee B3
MTD
MTD
MTD
MTD
MTD
Erosional surface
Erosional surface 2
BSR
Faults
Faults
Acoustic chimney
1 km
100 m
amplitude
14837
5568
-3701
-12970
B) P-wave velocity analysis of Line HR34a
HR34a
W
Crest
Reference area inside
The predicted GHRZ
BSR
Velocity (m.s-1)
2200
2000
1800
1600
1400
1200
1000
C) Line PL01PR07
Crest
Levee D
Levee C
Levee B3
Internal levee
scarp
MTD
Erosional surface
BSR
1 km
1.0
1.2
1.4
(s twt)

Fig. 13. Cross profile of channel complex B. A) The high-resolution seismic Line HR34a (for location see Fig. 3B) shows the characteristics of the eastern side of channel complex B with the staircase shape of the erosional surface, the internal levee overlying the MTD resulting from the collapse of levee B3. Note: the so-called Crest above the top of levee B3 and the chaotic facies of the enigmatic mass; the set of faults below the BSR and faults below the Crest; the second erosional surface (yellow color line) and associated MTDs below the last one; B) P-wave velocity analysis of Line HR34a. Note: the velocity range (1900-2050 m/s) which characterize the GH just above the BSR and the low velocity values (1200-1500 m/s) which indicate the presence of free gas-bearing sediments below the BSR; the reference area inside the predicted GHSZ where no BSR is observed, neither positive or negative velocity anomalies and gas-related seismic signatures (from Ker at al., 2019). C) The SYSIF PL01PR07 profile (for location see Fig. 3B) shows the normal fault that crosses the BSR, the erosional surface with scarps and the levees B3, C and D and overlying upper sedimentary layers up to the seafloor. Note the well expressed MTD and the wedge-shaped internal levee with overlying upper deposits.

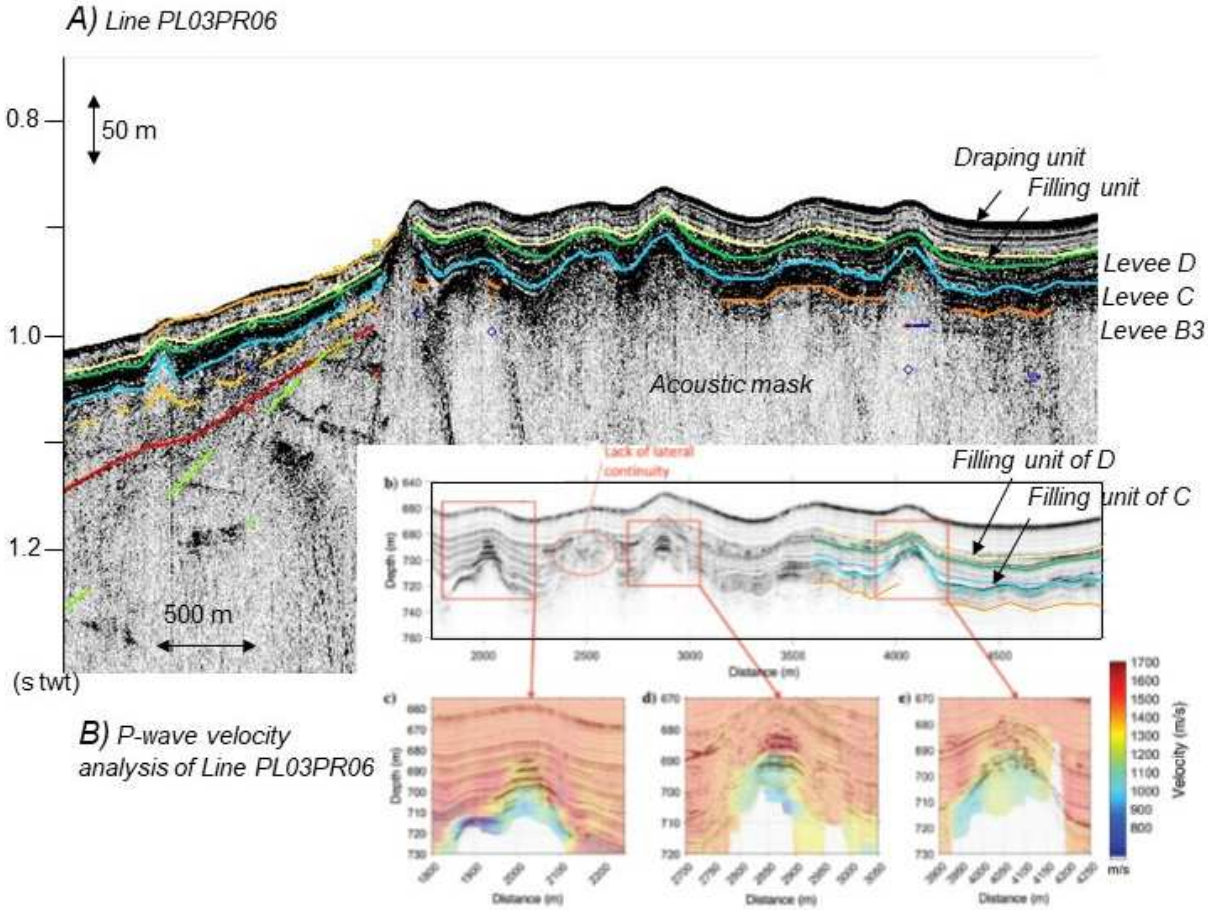

Fig. 14. Presence of gas within levees C and B3. A) The SYSIF PL03PR06 profile (for location see Fig. 3B) shows an acoustic mask at the top of levee B3 and chaotic facies within levee C. B) SYSIF profile migrated and Velocity analysis. The low-acoustic-velocity areas correspond to crests of sedimentary undulations of levee C filled with gas (Colin et al., 2020a).

The map of the successive channel-levee systems B0 to the youngest shows their extent within paleo-valley B and on the slope of the study area (Fig. 15A-F). However, B0 to B2 were difficult to map due to the scarcity of HR profiles. The two paleo-valleys C and D have developed northeast of paleo-valley B and have fed channel complexes (Fig. 3A). Only two channels of these complexes, called channel C and channel D, were studied. These channels lie directly over the widespread MTD12 and sometimes over-incise it. (Fig. 15A).

532 The levees of channels C and D have a wide extent (12 km) and well-stratified deposits and
533 their distal parts overlap the internal levee coeval to channels B4 and B5 (Fig. 8). These
534 levees have been mapped using all seismic datasets (Fig. 15G-H).

535 • Paleo-valley Y is located at the seafloor between the Danube canyon and paleo-
536 valley A (Fig. 2; Fig. 3A). Channel Y appears over channel A and over channel complex B
537 (Fig. 11). However, the seismic data are insufficient to map channel Y and to determine its
538 location either between channel complex B and channel C or between channel D and the
539 youngest Danube channel.

540 • Paleo-valley Danube is located southwest of paleo-valley A. The most recent
541 Danube channel-levee system is observed from the slope to the basin (unit 4 from Popescu
542 et al., 2001) and crosscuts the distal parts of channel complexes B to D (Fig. 2; Fig. 17). This
543 observation implies that the most recent Danube channel is younger than these channel
544 complexes, in agreement with Hillman et al. (2018). Westward, the most recent Danube
545 channel appears over possibly channel A and channel Z. According to Hillman et al. (2018),
546 Z would be below the erosional surface and very old (> 1 Ma) (Fig. 17).

547

548

549

550 .

551

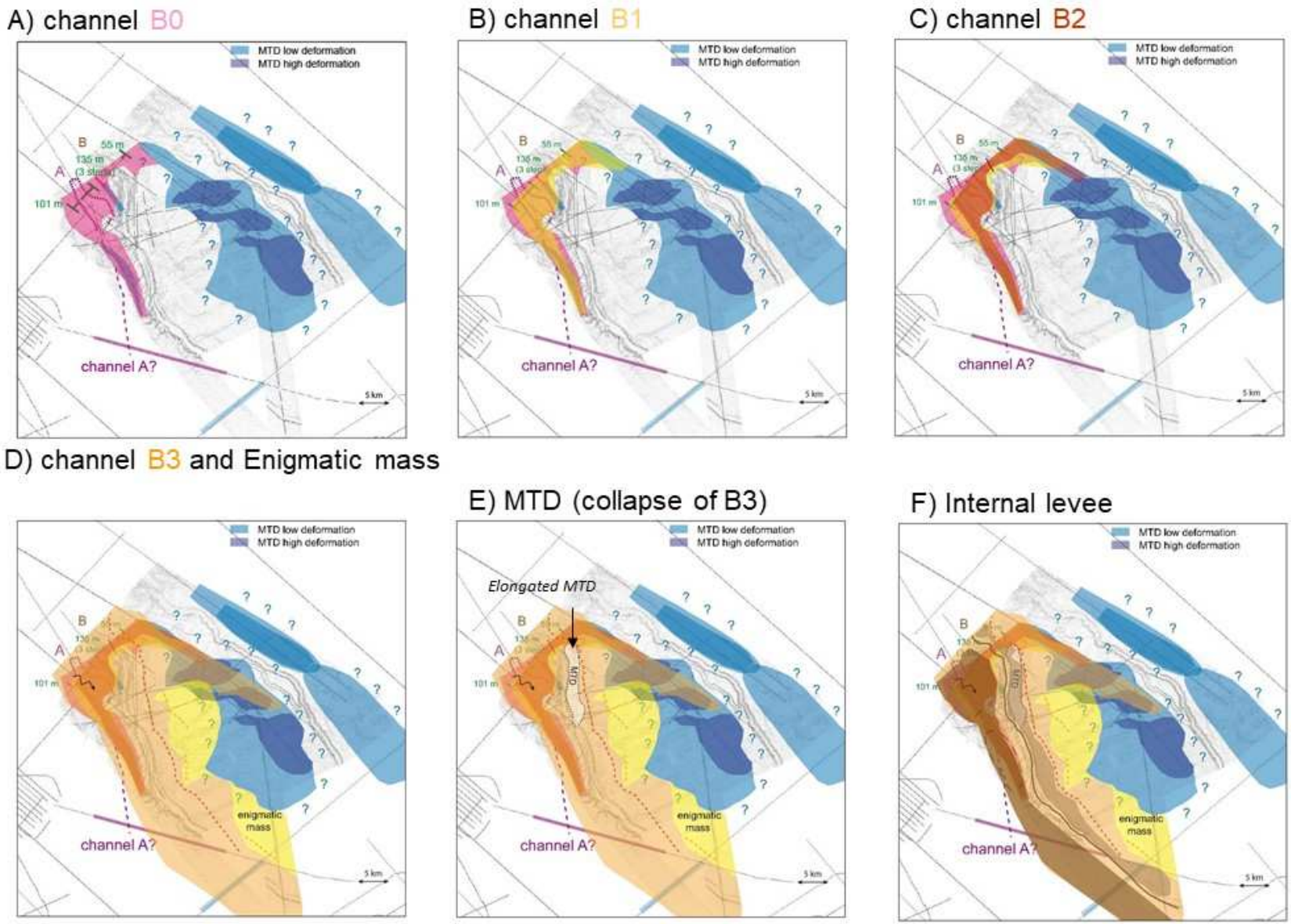
A) channel B0
B) channel B1
C) channel B2
D) channel B3 and Enigmatic mass
E) MTD (collapse of B3)
F) Internal levee
MTD low deformation
MTD high deformation
channel A?
enigmatic mass
Elongated MTD
5 km

552

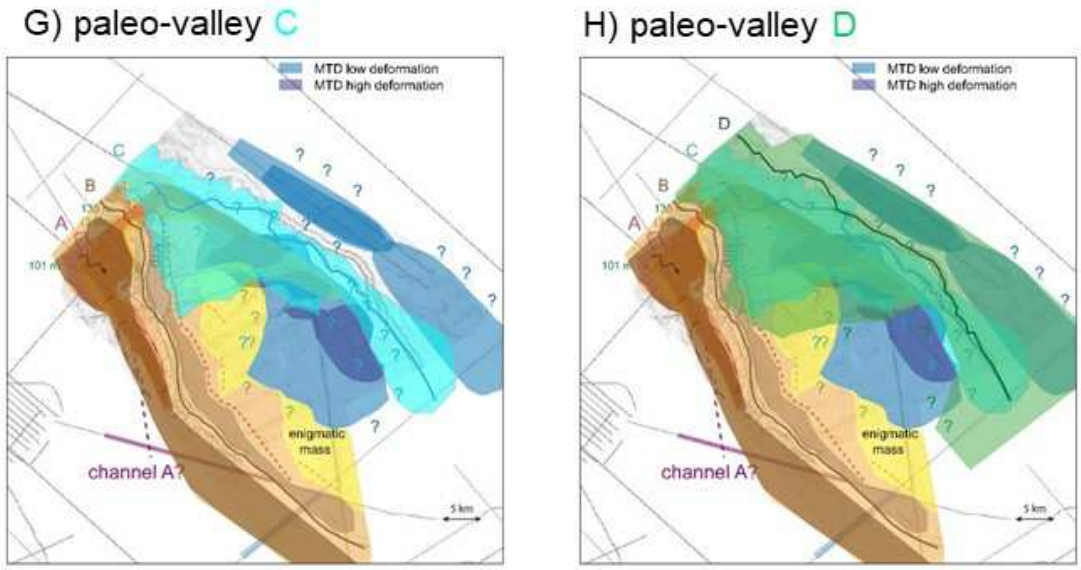

Fig. 15. Extent of channel-levees systems of Paleo-valley A, channel complex B, C and D (see location of the map on Fig. 3). MTDs on the erosional surface (blue polygon) and lateral scarps of erosional troughs A and B have been reported (green color). The axes of channels are marked by a line of the same color as the color of the levees. The levee extent is indicated by a colored polygon. The channel-levees are successively stacked on the different maps. A) Valley A and possible channel A (purple color) Channel-levees B0 (pink color); B) Channel-levees B1 (yellow color) over B0; C) Channel-levees B2 over B0 and B1; D) Channel-levees B3 over B0, B1 and B2 and Enigmatic mass interpreted as belonging to the levee B3; E) elongated MTD resulting from the collapse of B3 eastern levee; F) Internal levee on the elongated MTD and channel-levees B0 to B3. G) Channel-levees C (turquoise blue color); H) Channel-levees D (green color). The maps are based on

562 *only HR lines for channel-levees B0 to B2 and on all seismic profiles (HR, SYSIF, SDS) for channel-levees B3, C, D, the elongated MTD and*

563 *the internal levee.*

564

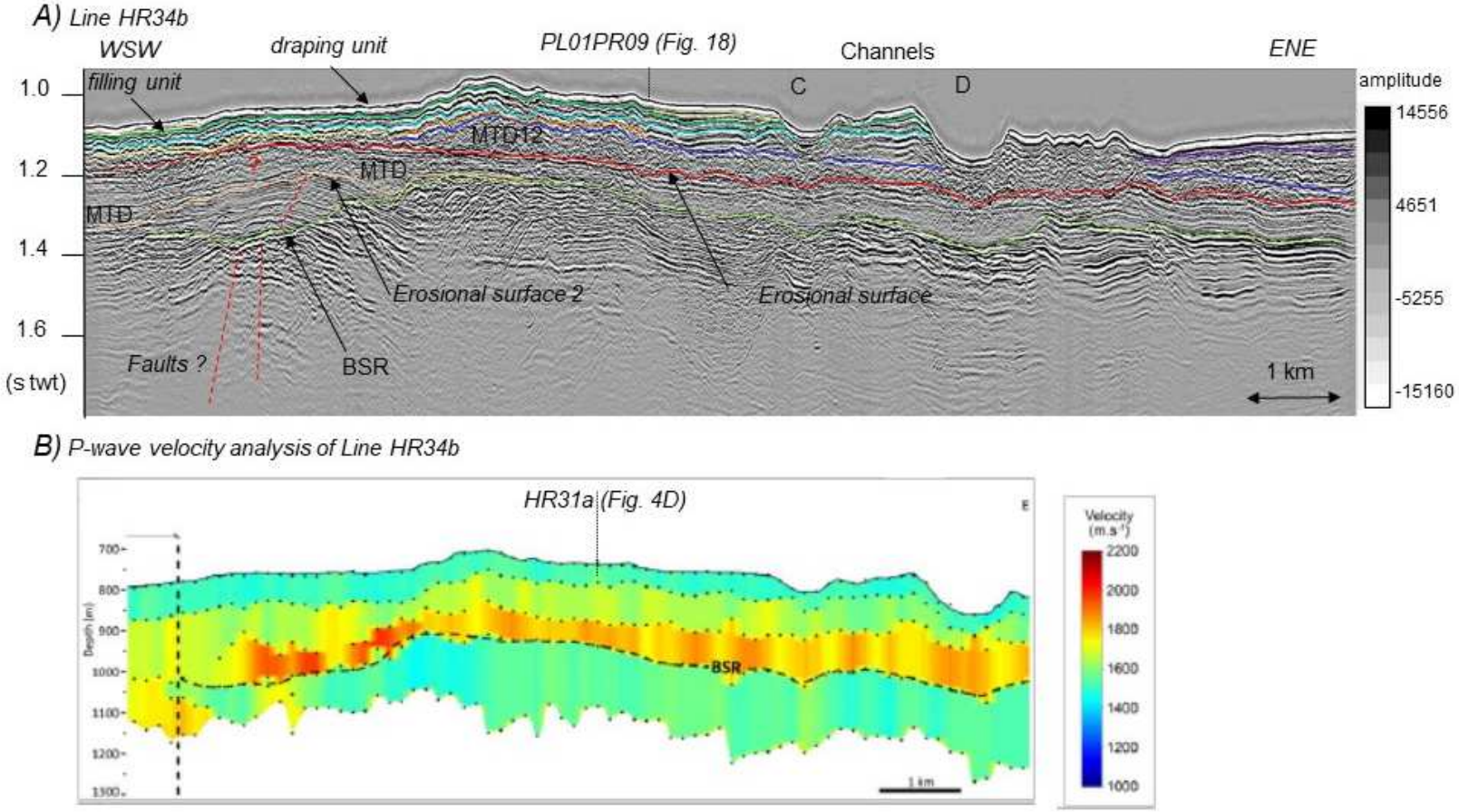

565

Fig. 16. Cross profile of channel-levees C and D. The high-resolution seismic Line HR34b (for location see Fig. 3B) shows these channel-levees which lie directly on MTD12.

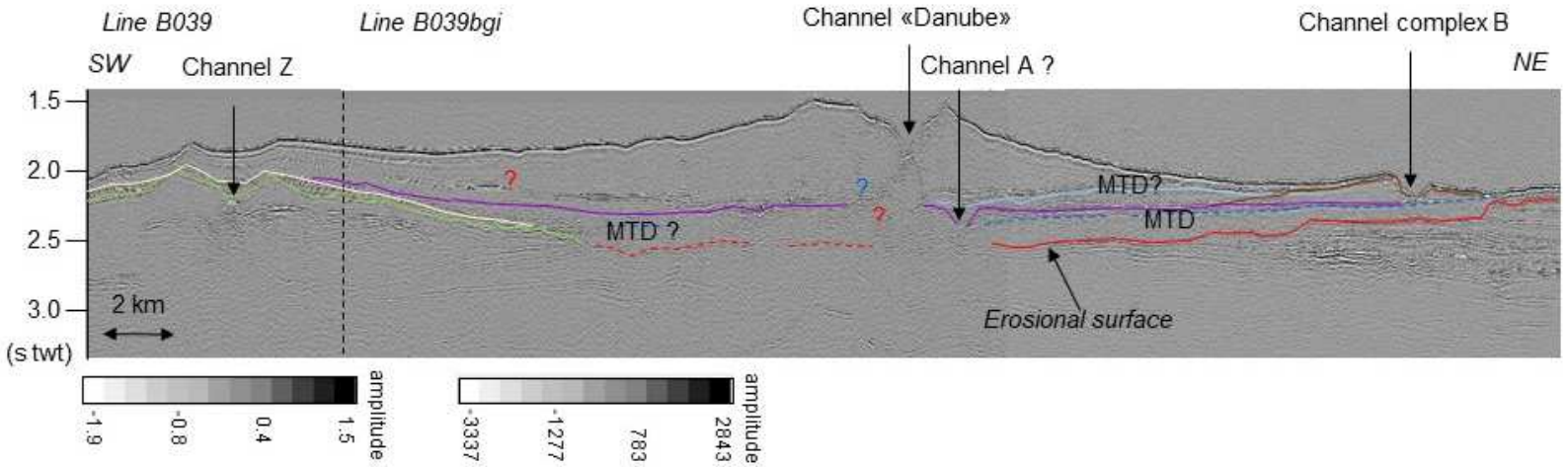

Fig. 17. Cross profile of channel "Danube". A) The high-resolution seismic Line B039bgi (for location see Fig. 3B) shows the youngest channel-levee "Danube" which lie, respectively from SW to NE, over an infill unit of channel Z, possibly channel A, an MTD (in light blue) and, channel complex B. Note the erosional surface and overlying MTD (in dark blue).

The chronology of paleo-valleys and their connected channel complexes is based on the principle of superposition. Channel complex B crosscuts paleo-valley A and is partially covered by the distal part of the levees of channels C and D (Fig. 8). The activity of paleo-valley A is continuous during the construction of channel complex B as revealed by the small channels affecting levee deposits to the seafloor where channel A crosscuts channel complex B (Fig. 3A). Channel D crosscuts channel C (Fig. 15H). The resulting chronology of paleo-valleys is, from the oldest to the youngest, A, B, C, D, and the most recent, the Danube paleo-valley which is connected to the youngest Danube channel.

The end of activity of paleo-valleys A, B, C, and D is marked by a unit of up to 30 m thickness showing low amplitude infilling seismic facies (Fig. 18). This infilling is attributed to late-stage distal overbank deposits from younger channels, such as possibly channels Y and Danube. The study area is covered by an almost draping unit (Fig. 18). This unit has been described from the core GAS-CS01 (GHASS survey) by Martinez-Lamas et al. (2020) as laminated clayey sequences that resemble the lacustrine varves of Degens et al. (1978). These lacustrine sequences have been interpreted as hyperpycnites i.e. hyperpycnal turbidites produced by discharges of the Danube river at the end of the glacial period (ca.33-17 ka) (Martinez-Lamas et al., 2020). We note that only 1 m of marine sediments has formed since the last connection to the Mediterranean Sea.

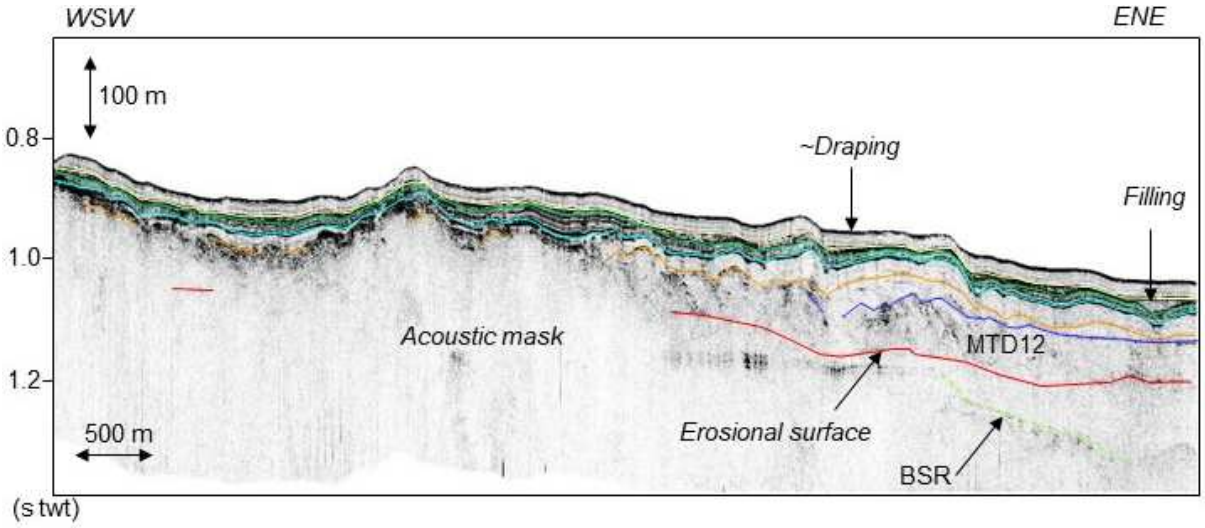

Fig. 18. Filling and draping upper sedimentary layers. The SYSIF PL01PR09 profile (for location see Fig. 3B) shows the unit (light yellow color) filling the underlying topography of the top of levee D (green color). The overlying draping unit outcrops at the seafloor. These two upper units act as a seal for upward gas migration as gas flares do not occur in this area (see Fig. 3A).

4.4 Surficial sediment instabilities

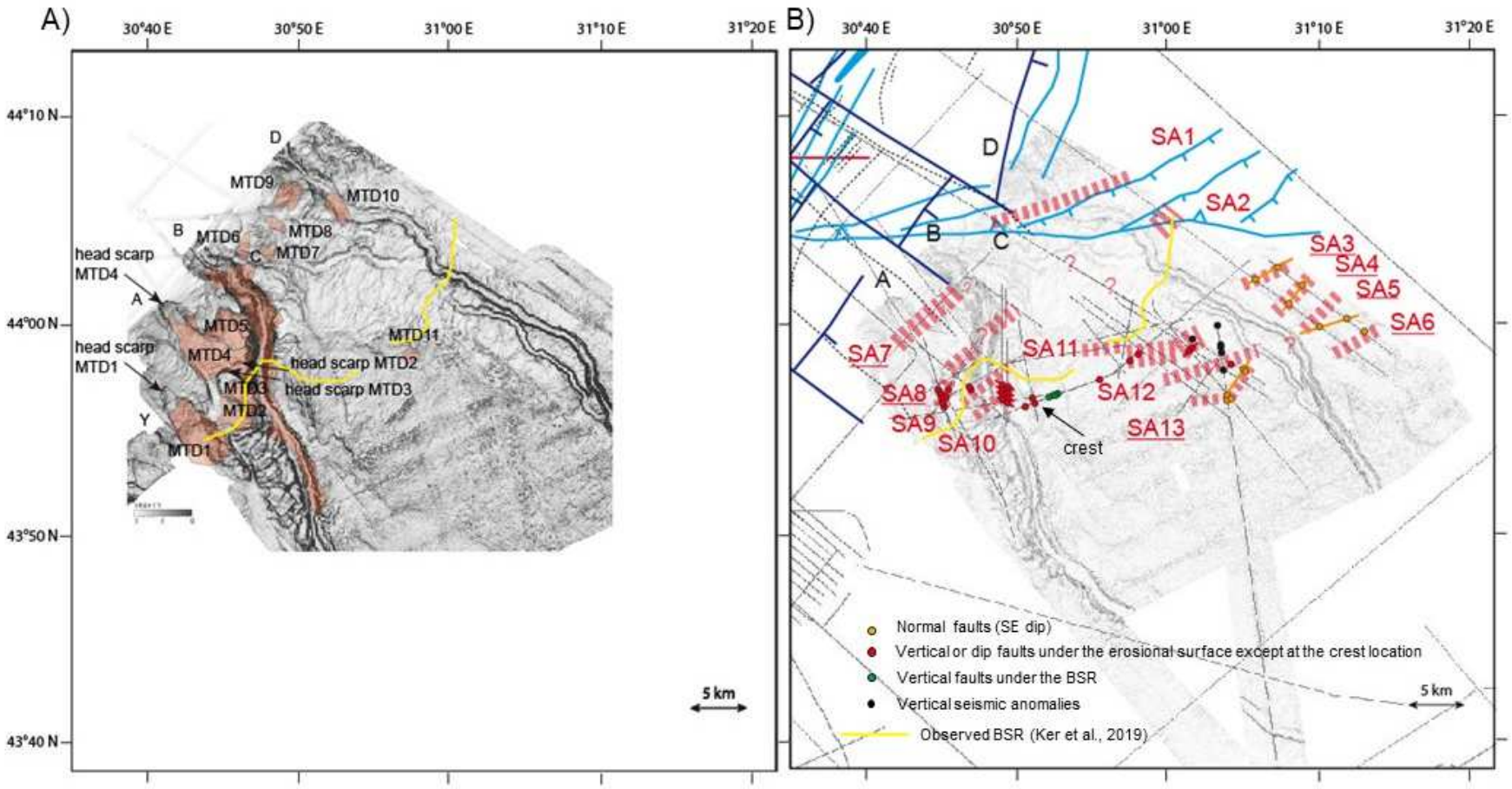

Fig. 19. Superficial MTDs and Fault pattern (see location on Fig. 3). A) Map of the superficial MTDs observed on SBP, SYSIF and/or HR seismic (red polygons). MTD1 appears within paleo-valley Y, MTD2, MTD3 and MTD4 within paleo-valley A with a retrogressive pattern, MTD5 is located between paleo-valleys A and B, MTD6 to MTD10 lie on the upper slope, and MTD11 on the middle slope. Note the MTDs on the walls of paleo-valley B

As mentioned previously (section 2.3), the seafloor surface is disturbed by scarps and associated MTDs linked to instabilities. Numerous MTDs disturb the superficial sediments of the headwalls and lateral walls of canyons/paleo-valleys A and B. The walls of channels along their entire length are also disturbed. Eleven MTDs located on the upper slope have been identified on seismic profiles and mapped (Fig. 8B, Fig. 19). In paleo-valley A, three distinct MTDs (MTD2 to MTD4) and their associated head scarps have been identified. MTD2 is at around 10 mbsf, reaches 35 m in thickness, and 2 km^2 in extent (Fig. 10 and Fig. 8B). MTD3 is at around 2 mbsf, reaches 25 m in thickness, and 3 km^2 in extent (Fig. 8B). MTD4 is at the seafloor and extends over a 9 km^2 area (Fig. 9). The three distinct MTDs suggest three main episodes of instability in a retrogressive pattern. It is worth noting that MTD5 could have occurred between MTD3 and MTD4 but this has not been identified in the seismic data (Fig. 19). Superficial MTDs can appear at the top of the field of the sediment wave revealing a decollement surface at the base of the draping unit (Fig. 10B).

4.5 Gas signatures and hydrates in upper sediments

As mentioned previously (section 2.3), the BSR occurs between ~700 and 1830 m water depth and its edge, i.e. its most landward termination (see Fig. 10 for an example), ranges in the predicted GHSZ (Popescu et al., 2004; Ker and Riboulot, 2015; Riboulot et al. 2017) (Fig. 3A). Gas signature is generally absent within the sediments located above the BSR (e.g., Fig. 5C), as confirmed by the velocity analysis of SYSIF data (Colin et al., 2020a) (Fig. 4D), and the absence of gas flares at the seafloor (Fig. 3A). However, there is one exception along the so-called Crest area where faults cross the BSR and, outcrop at the seafloor and feed gas flares (Ker et al., 2019). Velocity analysis of SYSIF data (Colin et al., 2020a) shows the presence of gas below the BSR under the Crest (Fig. 13B). These observations highlight that gas hydrates play the role of an efficient seal layer in controlling gas-flare distribution.

635 Under the BSR, rare observable vertical columns of seismic anomalies with a pull-down
636 effect, are interpreted as a localized accumulation of gas implying potential gas breaks
637 through the sediments (Fig. 6 below SA12; Fig. 12). Others seem to show a slight vertical
638 offset of reflectors suggesting potential faults. Acoustic chimneys also occur below the BSR
639 and mainly westwards of channels C and D (Fig. 6).
640 In the free gas area at the landward termination of the BSR, most of the columns of seismic
641 anomalies generally associated with underlying acoustic chimneys occur in levees
642 associated with channels B to D (Fig. 4B). They do not reach the seafloor but stop at the
643 level of the infilling unit and overlying draping lacustrine and marine sediments (Fig. 18).
644 Velocity analysis revealed the presence of free gas in the crests of sedimentary undulations
645 (Colin et al., 2020a). In our study, these crests have been correlated to levees B and C. (Fig.
646 14B. This confirms that the draping unit, and possibly the infill unit, bounds the upper limit of
647 the gas front and consequently plays the role of a seal layer. Most of the gas flares are in
648 association with sedimentary discontinuities such as the edge of canyon B and the paleo-
649 valleys and channel sidewalls (B, C and D), and slide scars (Fig. 3A). This is reminiscent of
650 Skarke et al. (2014).
651
652 4.6 Fault patterns and distribution
653
654 A couple of faults have been identified from seismic profiles (Fig. 19B). They appear as
655 single faults or sets of faults. The single faults are sometimes listric (Fig. 5B), with some of
656 them showing a normal vertical displacement of seismic reflectors (Fig 6, below SA13). The
657 sets of faults include small-offset and high-angle to vertical faults (Fig. 6, below SA1; Fig. 9,
658 below SA9). They are sometimes associated with acoustic chimneys which suggest the
659 presence of gas (Fig. 13A, below the so-called Crest). Some faults coincide with a major dip
660 change in stratification on both sides of the vertical columns of seismic anomalies (Fig. 6,
661 below SA13; Fig. 10, below SA8).

These faults are not randomly distributed in the study area or the sediment stratigraphy (Fig. 19). Almost all these faults affect sediments below the basal regional unconformity. Only the fault system of the Crest seems to have propagated to the seafloor within the surficial sediments (Fig. 13). This fault zone feeds gas flares and seems deep-seated even if its termination was not identified due to lack of penetration of the seismic signal (Ker et al., 2019). The eastern area is characterized by deeply rooted normal faults below the scarps of the basal unconformity. These faults sometimes become listric toward the BSR zone (Fig. 5B; Fig. 6). Sets of vertical faults occur below the BSR and at the BSR edge (Fig. 13A; Fig. 9, below SA9 and Fig. 10, below SA8), but few examples are observed cutting it (Fig. 12, below SA10). We note that this set of vertical faults seems to limit a free-gas zone below a marked BSR from a diffusegas zone without a BSR from either side (Fig. 13A). Upstream the BSR edge, the presence of gas facies and acoustic chimneys on seismic profiles does not allow us to identify faults directly (Fig. 4C). However, the abundance of faults reported on the shelf (see Fig. 3A) infers the presence of faults within the free-gas area (Fig. 19B).

Precise characterization of fault orientation is not possible in the study area with such a low coverage of HR seismic acquisition (Fig. 3). In the western zone, only a set of small offset faults with a NW-SE orientation can be determined from the correlation of closely spaced and parallel seismic lines along the east side of valley B (Fig. 19). We note that most of the vertical structures are observed from NE-SW seismic lines which could be consistent with transfer structures having a rough NW-SE orientation. In the eastern zone, the high-angle normal faults have NE-SW-oriented alignments.

5. Discussion

On the Dnepr paleo-delta in the NW Black Sea, it has been demonstrated that morphology, underlying stratigraphy, sediment properties, and the presence of gas hydrates control the distribution of gas flares (Naudts et al., 2006). Our results are similar. We show that the

690 extent of the BSR, faulting patterns, and arrangement of architectural elements such as
691 canyons, channel-levees, slide scars, and MTDs control the distribution of seal layers and
692 sedimentary discontinuities and consequently gas-flare distribution. However, we cannot
693 exclude that seepage may be primarily associated with tectonically driven flows through
694 regional faults (Kruglyakova et al., 2004). Moreover, the release of seismic energy during
695 earthquakes could cause slope failures and subsequent gas escape along slide scarps.
696 Further investigation of the deep fluid plumbing system and sediment properties remains
697 essential to discuss the factors controlling gas/fluid migration pathways and consequently
698 gas-flare distribution.
699 This work highlighted the evolution of the tectonic-sedimentary architecture of surficial
700 deposits and its impact on sediment instabilities, which is discussed below.
701
702 5.1 Origin of the Basal erosional surface and sediment instabilities
703
704 The basal erosional surface with the associated layer of MTDs is observable from the upper
705 continental slope down to the deep basin (Popescu et al., 2004; Winguth et al., 2000;
706 Hillmann et al., 2018). This erosional surface corresponds to the Base Neoeuxinian
707 Sequence Boundary of Hillman et al. (2018) attributed to the Würmian with a minimum
708 lake/sea level drop (about -130 m) at around 18000 BP (Panin and Jipa, 2002). The Base
709 Neoeuxinian Sequence Boundary has been recently dated using 14C dating, at a minimum
710 of ~22 ka (Lericolais et al., 2013) and was considered to mark the onset of activity in the
711 Danube Fan during the last sea-level lowstand in the Black Sea (Popescu et al., 2001).
712 However, the correlation with core Gas-CS01 (base of the draping unit) indicates the age at
713 a minimum of 32 ka (Martinez-Lamas et al., 2020). The presence of several built and
714 abandoned channel-levee systems between this draping unit and the basal erosional surface
715 suggests that this unconformity is significantly older.
716 It is generally considered that during sea-level falls, migration of the river-mouth to the shelf
717 edge and rapid deltaic sedimentation leads to an increase in sedimentation load,

718 overstepping and overpressuring in the prodelta and slope sediments, resulting in sediment
719 failure, MTD formation, and canyon development (Weimer, 1990; Posamentier and Kolla,
720 2003, Madof et al., 2009). A link between the MTDs, the scarp alignments of the basal
721 erosional surface, and the faults has been observed (Fig. 7B). The presence of normal faults
722 under SA3, SA4, and SA6 suggests that these sediment instabilities are related to normal
723 faults underneath, potentially of gravitational origin. Major dip changes in stratification at
724 SA7, SA8, and SA13 are also likely attributed to faults since these scarps are almost parallel
725 to the mapped SW-NE oriented faults from Konerding et al. (2010) (in dark blue on Fig. 19B).
726 We highlight that the observed faults are mainly located below the basal unconformity and
727 are mainly absent in the surficial deposits. This observation suggests that the faulting was
728 predominantly active before or during basal erosional surface formation. We also note that
729 the upper extensive parts of the MTDs lie over the scarp alignments whereas the
730 compressive bulges are downstream (e.g. Fig. 4C). The contribution of fault activity is
731 therefore identified as significant on slope failures and distribution of MTDs.
732 Sea-level falls may cause an additional effect, such as a reduction in hydrostatic pore
733 pressure in the fluid reservoir that lowers gas solubility and results in gas exsolution. The
734 subsequent accumulation of gas in porous layers interbedded within less permeable layers
735 prevents fluid escape (Magara, 1978; Lafuerza et al., 2009) and facilitates overpressure
736 build-up, which drives fluids along permeable migration pathways (e.g. faults), and may
737 cause a drop in the effective stress of the sediment and favour its failure (Bolton et al., 1998;
738 Dugan et al., 2003; Canals et al., 2004). Reactivation of inherited faults is also possible and
739 the subsequent fluid migration along them may contribute to the initiation and location of
740 surficial sediment instabilities. This potential fault reactivation during sea-level fall does not
741 exclude deep movements of over pressured layers at the regional scale. Indeed, examples of
742 gravity-driven deformations have been demonstrated on the Plio-Pleistocene time scale in
743 several deltaic settings characterized by underlying over pressured layers (dos Reis et al.,
744 2005 for the Gulf of Lion; Knox and Omatsola, 1989 and Rouby et al., 2011 for the Niger
745 delta). We note that regional-scale tectonic influence, such as the flexural uplift of the

746 Carpathians foreland due to the Wallachian deformations, cannot be excluded from this fault
747 activity along the Romanian margin (Cloetingh et al., 2003).
748 It is worth noting that the presence of an older erosional surface (erosional surface 2 in Fig.
749 13A) with associated MTDs, suggests a recurrence of significant instabilities possibly during
750 successive sea-level falls. Glacial and interglacial conditions control the alternating
751 turbidite/hemipelagic deposits and may explain the recurrence of slope failures. This has
752 been demonstrated for the Gulf of Lion where repeated slope failures occurred during glacial
753 periods at specific stratigraphic levels which correspond to weak layers between clay-rich
754 and turbidite sediments (Badhani et al., 2019, 2020).
755
756 5.2 The channel-levee systems: Impact of fault systems and instabilities
757
758 The data highlight the build-up of channel-levee systems above the basal layer of MTDs and
759 the Neoeuxinian sequence boundary (Fig. 15). This suggests that fluvially derived sediments
760 were transported directly into canyon heads and then as channelized turbidity flows thanks to
761 the connection between fluvial valleys incised in the shelf and canyons. The vertical
762 succession from MTDs to channelized deposits is reminiscent of the “deep-water sequence”
763 of Weimer (1990). The model of Winguth et al. (2000) for the Danube and Dniepr fans can be
764 applied to the study because it is based on the depositional model of Weimer (1990) for
765 deep-sea fan systems, in which sea-level fluctuation controls fan development. We have
766 integrated the tectonics and gas/gas-hydrate dynamics which contribute to sediment
767 instabilities, into the model of Winguth (2000) and propose a diagram of the evolution of the
768 study area since the last sea level fall (Fig. 20). During the sea-level fall, gravity-driven
769 tectonic and/or fault reactivation with subsequent gas expulsion are invoked to trigger major
770 sedimentary instabilities of the slope leading to the formation of MTDs (Fig. 20A). Then
771 during lowstands, the fan system becomes the main site of deposition, and coarse material is
772 confined to the channels, whereas finer material is swept onto the levees and beyond to form
773 overbank deposits (Fig. 20B).

774 The relative chronology of paleo-valleys (see section 4.3) shows that the turbidite activity
775 migrated northward from paleo-valleys A to D and then southward from paleo-valley D to the
776 Viteaz canyon. We suppose the low sedimentary load on the shelf to be insufficient to induce
777 gravity-deformation and subsequent fluid/gas expulsion.
778 Sediment instability during canyon activity is related to both erosive action within the canyon
779 (sediment flow dynamics) and the presence of gas in surficial deposits (high sedimentation
780 rate or migration from a fault system). Sediment instabilities were observed during canyon
781 activity and formation of the erosional surface (Fig. 7B) but also during the formation of
782 channel-levee systems (Fig. 8). According to Hillmann et al. (2018), the slope failure located
783 on the western wall of paleo-valley B and labeled slump S2 by these authors shows no
784 evidence for deposits downslope or in the canyon that could be related to this event. This
785 suggests that the canyon was active at the time of slope failure. Our results show the same
786 phenomenon for paleo-valley A, for which the complete removal of sediments within this
787 valley suggests strong turbiditic activity during slope failure. Undercutting at the toe of a
788 slope due to erosive action of turbidity currents in canyons may result in the axial incision of
789 the canyon floor, triggering slope failure. Overpressure generation due to rapid deposition of
790 slope sediments may have also contributed to slope instability (Hillman et al. 2018). It is likely
791 that, in the Viteaz (Danube) turbidite system, the location of gassy facies within the canyon
792 and the upper part of the associated channel favored instability and possibly triggered
793 sediment failures (Popescu, 2002, e.g. Egorov et al., 1998 for the Dnepr Canyon). Gas
794 migration from faults could also contribute to this fluid overpressure and related sediment
795 instability in canyons. The collapse of the eastern levee of channel B3 (Fig. 12) and the
796 sedimentary deformation of the levee, i.e. the enigmatic mass (Fig. 13), are suspected to be
797 attributed to the gas flow observed from the Crest fault system. We, therefore, hypothesize
798 that the combined effect of significant turbidite activity (at least in paleo-valleys A and B) and
799 the presence of gas at the walls of canyons and valleys influences sediment stability and the
800 concurrent development of canyons and/or paleo-valleys A to D (Fig. 20B).
801

802 5.3. Surficial sediment deposits and instabilities

803

804 The surficial infilling and draping units mark the abandonment of canyon-channel systems in
805 the study area and migration of the turbidite activity to the south, i.e. within canyon Y and/or
806 Danube (Viteaz) canyon/valley. These units record the last evolution of the Danube river
807 activity linked to the Alpine ice-sheet fluctuations during the end of the last glacial 33-17 ka
808 BP (lacustrine deposits, Martinez-Lamas et al., 2020), the last connection to the Marmara-
809 Mediterranean Sea with sapropel and carbonates (Constantinescu et al., 2015) and marine
810 sedimentation. This evolution from channel filling to marine sedimentation suggests a
811 retrogradation of the deltaic system towards the coast during the sea-level rise and is
812 consistent with the conventional sequence stratigraphic models (Mitchum and Vail, 1977;
813 Vail et al., 1977; Van Wagoner et al., 1988) (Fig. 20C).
814 Some MTDs are recorded within the draping unit along the upper slope, within the free-gas
815 area, and in zones favorable to failure initiation such as the flanks of paleo-canyons and the
816 sediment-wave area (Fig. 19; Fig. 10). According to Lericolais et al. (2009), the Melt Water
817 Pulse 1A at 12.5 ka ^{14}C BP is the source of water level rise between -40 to -20 m below the
818 present-day sea level. Then, during the low water level stage from 11 to 8 ka ^{14}C BP (i.e.,
819 younger Dryas), a lacustrine sedimentary wedge system prograded on the Romanian shelf to
820 the Danube canyon head. It is likely that this enhanced sediment supply onto the shelf led to
821 abrupt overloading generating a new and short episode of gravity-deformation and
822 subsequent fluid/gas expulsion underlying slope instabilities.
823 Sea level has been rising and the Danubian sediment supply decreasing since around 8 kya
824 (Panin and Jipa, 2002). The present-day depocenters in the region are the Danube delta
825 front and prodelta areas on the internal shelf i.e. to 50-60 m depth. According to Winguth et
826 al. (2000), during highstands, the deltaic region is far removed from the shelf edge and is the
827 depocenter for much of the fluvial sediment input. The slope and basin are sediment-starved
828 so that a condensed section is laid down as a result of hemipelagic deposition (Fig. 20D).
829 Sea level is still rising and outpaces subsidence within the coastal area of the Danube delta

(Panin et al., 1983). This suggests that sedimentary load on the shelf is too low to induce present-day gravity-driven deformation. However, rapid sea-level rise is well known to induce bending stress on the continental slope, which can lead to elevated seismicity and potential fault reactivation that can consequentially trigger landslides (Brothers et al., 2013). This could explain the origin of sub-surface MTDs, i.e., those buried under marine sediments (around 1 m thick from GAS-CS01, see section 4.3).

5.4. Potential role of seismicity and gas-hydrate dynamic on sediment instability

Of the mechanisms which can trigger sediment instabilities throughout geological recording are the seismic activity linked to the regional faulting pattern, the presence of gas in the sediment and the dissociation of gas hydrate (see Garziglia et al., 2008 for similar investigation for the Nile delta).

In the study area, earthquakes of magnitude > 7 have occurred along the Romania-Bulgaria coast and could have caused submarine slides and consequential tsunamis. For example, two earthquakes of magnitude = 7.1 and 7.2 were reported offshore NE Bulgaria (Papadopoulos et al., 2011), and near the Sugar canyon (Matova, 2000), respectively (Fig. 2 and Table 1). In the study area, a magnitude 3.9 earthquake occurred in 2007 at the location of the W-E oriented fault (Fig. 2 and Table 1,). Two other earthquakes of magnitudes 4.6 and 4 occurred further offshore the study area in 1986 and 2009 respectively. Despite their low magnitude, these earthquakes could have triggered surficial sediment instabilities, especially along the valley flanks such as for paleo-valleys A and B and also the deformation of levee B3, i.e. the enigmatic mass. Earthquakes of higher magnitude could occur in the study area. The role of paleo-seismic activity in the initiation of MTDs is speculative but cannot be excluded, especially as scarp alignments and faults are spatially linked.

Another mechanism that can trigger sediment instabilities is gas hydrate dissociation and the subsequent free gas release (Bouriak et al., 2000; Bünz et al., 2005; Kwon and Cho, 2012). Several factors lead to gas-hydrate dissociation such as sea level fall (Haq, 1998; Maslin et

858 al., 1998, 2004; Kennett et al., 2003), penetration in the Black Sea of warmer Mediterranean
859 water during the rapid transgression after the Last Glacial Maximum (Zander et al., 2017;
860 Matenco et al., 2016), or salt diffusion within the sediment (Riboulot et al., 2018). Potentially,
861 the superficial sedimentary instabilities close to the BSR edge such as MTD1 are provoked
862 by gas hydrate dissociation (Fig. 19A). We also note the presence of normal faults which
863 seem to propagate listrically toward the BSR. They are then potentially related to free gas
864 release following the upward migration of gas hydrate since the last glacial maximum (Fig. 5,
865 below SA5) (Dillon et al., 1998). Listric faults can also induce slope instabilities, a process
866 that shaped these basin margins during Miocene-Pliocene times (Fig. 1B, Munteanu et al.,
867 2012). The field of sediment waves could also be interpreted as sediment destabilization by
868 dissociation of gas hydrate (Fig. 10). Indeed, the substratum of sediment waves corresponds
869 to the BSR. Moreover, the sets of vertical faults which coincide with the BSR edge (e.g. Fig.
870 9, below SA9) are more likely to be fractures linked to free-gas overpressure at the landward
871 termination of the GHSZ than tectonic structures. We add that, conversely, these fractures
872 can increase free-gas migration during BSR evolution and help gas-hydrate dissociation
873 along the landward termination of the GHSZ (Yang and Davies, 2013). In the Dniepr paleo-
874 delta, northward of the study area offshore Crimea, the role of gas hydrate dynamics on
875 slope failures remains unclear (Zandler et al., 2018). Nevertheless, because mass-wasting
876 processes occur on channel-levees upstream the GHSZ, slope failure could have been
877 facilitated by gas-hydrate destabilization (Naudts et al., 2006). As gas hydrate dissociation is
878 still in progress, the slope studied here is gradually weakening.
879

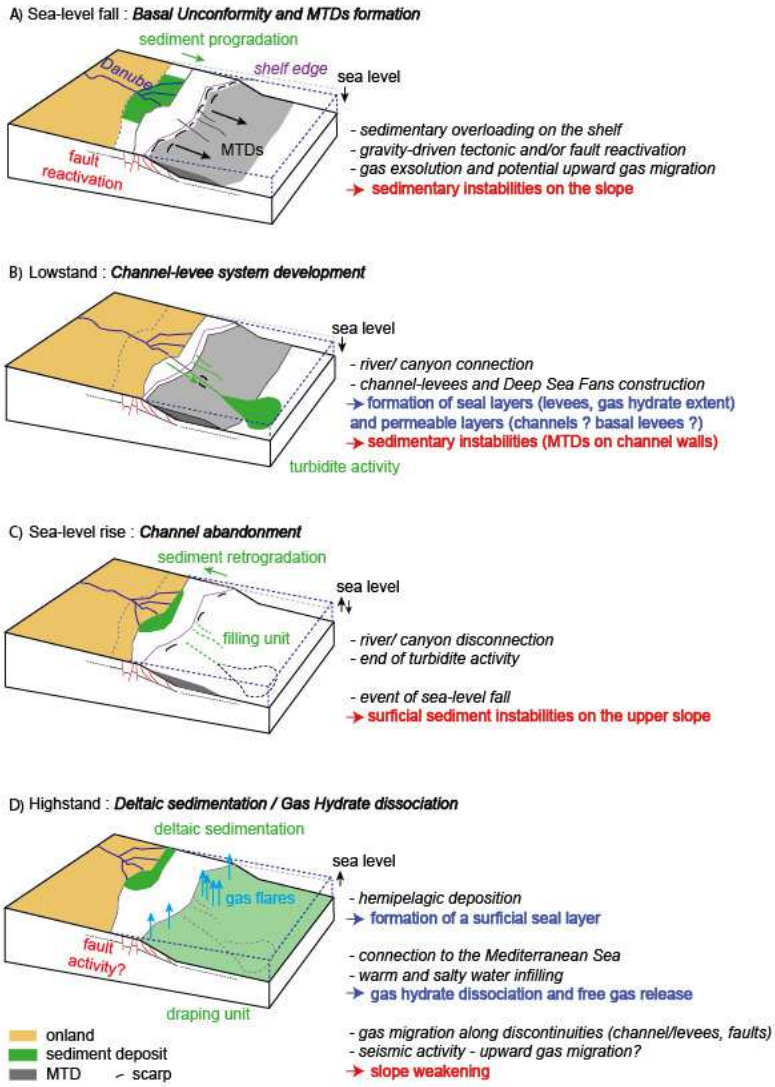

880

881 *Fig. 20. Evolution of the tectonic-sedimentary architecture of surficial deposits since the last*
882 *sea level fall. A) Sea level fall, formation of the basal erosional surface boundary and the*
883 *basal layer of MTDs. B) Lowstand and the development of the canyons and channel-levee*
884 *systems. Some sediment instabilities are also recorded within the canyon during this stage.*
885 *C) Sea-level rise and abandonment of the channel. Formation of the infilling and draping unit.*
886 *Development of the surficial MTDs during a short stage of gravity-driven instability. D)*
887 *Highstand with deltaic sedimentation and gas hydrate dissociation along the slope. The*
888 *present-day gas flare location is mainly controlled by the presence of gas hydrates, the*
889 *location of canyons and slide walls, the fault systems and the sealing draping unit.*

Conclusion

This work, based on the detailed analysis of multi-scale seismic data sets, has improved our understanding of the relationships between sedimentary architecture, faulting, slope instability, and fluid systems at the seafloor offshore Romania. The most recent paleo-valleys and their associated channel-levee complex/systems have formed over a basal layer of MTDs associated with an erosional unconformity attributed to the Base Neoeuxinian Sequence Boundary related to the last sea-level fall. The stacking pattern of these channelized systems shows that the turbidite activity migrated northward through at least five main paleo-valleys and then southward to the youngest Danube paleo-valley. The erosional unconformity shows slide scarp alignments, which generally coincide with normal to listric faults possibly linked to gravitational deformation. The geometry of paleo-valleys is strongly influenced by major sedimentary instabilities related to erosional processes and gas accumulation. Surficial (recent) sediment instabilities are interpreted as related to a gravity-driven fault reactivation attributed to the last melt water pulse and potential seismicity along the deep faults as well as gas hydrate dissociation.

The evolution from MTDs to turbidite and then marine deposits is consistent with the conventional sequence stratigraphy models that consider sea-level changes as the main control factor of margin sedimentation. However, gravity-driven deformation with possible seismicity and gas/gas-hydrate dynamics are considered as significant additional parameters impacting slope instabilities offshore Romania.

Acknowledgments

The officers and crew during the GHASS cruise on board R/V Pourquoi Pas? and the Genavir and Ifremer technical staff during and after the cruise are greatly thanked. S. Ker, V. Riboulot, B. Marsset, F. Colin, Y. Thomas are greatly thanked for their scientific and technical contribution. Andrew S. Madof and an anonymous reviewer are thanked for their comments that helped to improve this manuscript. We also thank the editor Liviu Matenco for his general comments. We sincerely thank Alison Chalm for revision of the English language.

Data availability

Data sets used in the current study were acquired during the GHASS expedition (10.17600/15000500) and data set information are available in the GHASS cruise report (http://archimer.ifremer.fr/doc/00300/41141).

References

Anton, E.M., Munteanu, I., Dinu, C., Melinte-Dobrinescu, M.C., 2019. Litho- and biostratigraphy of the Eocene deposits from Istria Basin northern edge (Western Black Sea). Geo-Eco-Marina. 25, 55-70.

Artemov, Y. G., Egorov, V. N., Polikarpov, G. G., Gulin, S. B., 2007. Methane emission to the hydro - and atmosphere by gas bubble streams in the Dnieper paleo-delta, the Black Sea (in Russian). Rep. Natl. Acad. Sci. Ukraine. 5, 110-116.

Artyushkov, E.V., 1992. Role of crustal stretching on subsidence of continental crust. Tectonophysics. 215, 187-207. https://doi.org/10.1016/0040-1951(92)90081-G.

Badertscher, S., Fleitmann, D., Cheng, H., Edwards, R.L., Göktürk, O.M., Zumbühl, A., Leuenberger, M., Tüysüz, O., 2011. Pleistocene water intrusions from the

944 Mediterranean and Caspian seas into the Black Sea. Nature Geosci. 4, 236–239.
945 https://doi.org/10.1038/ngeo1106.
946 Badhani, S., Cattaneo, A., Dennielou, B., Leroux, E., Colin, F., Thomas, Y., Jouet, G.,
947 Rabineau, M., Droz, L., 2019. Morphology of retrogressive failures in the Eastern
948 Rhone Interfluve during the Last Glacial Maximum (Gulf of Lions, Western
949 Mediterranean). Geomorphology. 351,.
950 https://doi.org/10.1016/j.geomorph.2019.106894.
951 Badhani, S., Cattaneo, A., Collico, S., Urgeles, R., Dennielou, B., Leroux, E., Colin, F.,
952 Garziglia, S., Rabineau, M., Droz, L., 2020. Integrated geophysical, sedimentological
953 and geotechnical investigation of submarine landslides in the Gulf of Lions (Western
954 Mediterranean). Geological Society, London, Special Publications. 500, 359-376.
955 https://doi.org/10.1144/SP500-2019-175.
956 Ballas, G., Garziglia, S., Sultan, N., Pelleter, E., Toucanne, S., Marsset, T., Riboulot, V., Ker,
957 S., 2018. Influence of early diagenesis on geotechnical properties of clay sediments
958 (Romania, Black Sea). Engineering Geology. 240, 175-188.
959 https://doi.org/10.1016/j.enggeo.2018.04.019Get.
960 Bega, Z., Ionescu, G., 2009. Neogene structural styles of the NW Black Sea region, offshore
961 Romania. The Leading Edge. 28, 1082-1089. https://doi.org/10.1190/1.3236378.
962 Bolton, A.J., Maltman, A.J., Clenell, M.B., 1998. The importance of overpressure timing and
963 permeability evolution in fine-grained sediments undergoing shear. J. Struct. Geol. 20,
964 8, 1013-1022. https://doi.org/10.1016/S0191-8141(98)00030-3.
965 Bouriak, S., Vanneste, M., Saoutkine, A., 2000. Inferred gas hydrates and clay diapirs near
966 the Storegga Slide on the southern edge of the Vøring Plateau, offshore Norway. Mar.
967 Geol. 163, 125-148. https://doi.org/10.1016/S0025-3227(99)00115-2.
968 Brothers, D.S., Luttrell, K.M., Chaytor, J.D., 2013. Sea-level-induced seismicity and
969 submarine landslide occurrence. Geology, 41, 9, 979-982.
970 https://doi.org/10.1130/G34410.1.

971 Bünz, S., Mienert, J., Bryn, P., Berg, K., 2005. Fluid flow impact on slope failure from 3D
972 seismic data: a case study in the Storegga Slide. Basin Res. 17, 109-122.
973 https://doi.org/10.1111/j.1365-2117.2005.00256.x.
974 Canals, M., Lastras, G., Urgeles, R., Casamor, J.L., Mienert, J., Cattaneo, A., De Batist, M.,
975 Haflidason, H., Imbo, Y., Laberg, J.S., Locat, J., Long, D., Longva, O., Masson, D.G.,
976 Sultan, N., Trincardi, F. and Bryn, P., 2004. Slope failure dynamics and impacts from
977 seafloor and shallow sub-seafloor geophysical data: case studies from the COSTA
978 Project. Mar. Geol. 213, 9-72.
979 Cloetingh, S.A.P.L., Burov, E., Matenco, L., Toussaint, G., Bertotti, G., Andriessen, P.A.M.,
980 Wortel, M.J.R., Spakman, W., 2003. Thermo-mechanical controls on the mode of
981 continental collision in the SE Carpathians (Romania). Earth and Planetary Science
982 Letters, 218, 57-76. https://doi.org/10.1016/S0012-821X(03)00645-9.
983 Colin, F., Ker, S., Marsset, B., 2020a. Fine-scale velocity distribution revealed by datuming of
984 very-high resolution deep-towed seismic data: Example of a shallow-gas system from
985 the western Black Sea. Geophysics. 85, 5, 161-172. 10.1190/geo2019-0686.1 1.
986 Colin, F., Ker, S., Riboulot, V., Sultan, N., 2020b. Irregular BSR: Evidence of an Ongoing
987 Reequilibrium of a Gas Hydrate System. Geophysical Research Letters. 47, 20.
988 https://doi.org/10.1029/2020GL089906.
989 Constantinescu, A.M., Toucanne, S., Dennielou, B., Jorry, S.J., Mulder, T., Lericolais, G.,
990 2015. Evolution of the Danube Deep-Sea fan since the last glacial maximum: new
991 insights into Black Sea water-level fluctuations. Mar. Geol. 367, 50-68.
992 https://doi.org/10.1016/j.margeo.2015.05.007.
993 Diaconu, A., Munteanu, I., Rădulescu, V., Moise, G., 2020. Gas escape features on the
994 Romanian Black Sea shelf - Examples from 2D seismic interpretation. Geo-Eco-Marina.
995 26, 1-9.
996 Dickens, G.R., and Quinby-Hunt, M.S., 1997. Methane hydrate in pore water: a simple
997 theorical approach for geophysical applications. J. Geophys. Res. 102, 773-783.
998 https://doi.org/10.1029/96JB02941.

999 Dillon, W.P., Danforth, W.W., Hutchinson, D.R., Drury, R.M., Taylor, M.H., Booth, J.S., 1998.
1000 Evidence for faulting related to dissociation of gas hydrate and release of methane off
1001 the southeastern United States. Journal of the Geological Society, London, Special
1002 Publications. 137, 293-302. https://doi.org/10.1144/GSL.SP.1998.137.01.23.
1003 Dinu, C., Tambrea, D., Raileanu, A., 2003. Transition from extensional to compressional
1004 structures in the Upper Miocene Shally deposits, Western Black Sea. AAPG,
1005 Barcelona.
1006 Dinu, C., Wong, H.K., Ţambrea, D. and Matenco, L., 2005. Stratigraphic and structural
1007 characteristics of the Romanian Black Sea shelf, Tectonophysics. 410, 417-435,
1008 doi:10.1016/j.tecto.2005.04.012.
1009 Dinu, C., Munteanu, I., Tambrea, D., Panin, N., 2018. Gas hydrates, Flares Seeps Offshore
1010 Romania, A Review. Geo-Eco-Marina. 24, 5-56.
1011 dos Reis, A.T., Gorini, C., Mauffret, A. 2005. Implications of salt–sediment interactions on the
1012 architecture of the Gulf of Lions deep-water sedimentary systems—western
1013 Mediterranean Sea. Marine and Petroleum Geology. 22, 713–746,
1014 https://doi.org/10.1016/J.MARPETGEO.2005.03.006.
1015 Droz, L., Marsset, T., Ondreas, H., Lopez, M., Savoye, B., Spy-Anderson, F.-L., 2003.
1016 Architecture of an active mud-rich turbidite system: the Zaire Fan (Congo-Angola
1017 margin southeast Atlantic) results from ZaïAngo 1 and 2 cruises. AAPG Bull. 87,
1018 1145e1168. http://dx.doi.org/10.1306/03070300013.
1019 Dugan, B., Flemings, P., Olgaard, D.L. and Gooch, M.J., 2003. Consolidation, effective
1020 stress, and fluid pressure of sediments from ODP Site 1073, US mid-Atlantic
1021 continental slope. Earth Planet. Sc. Lett. 215, 13-26. https://doi.org/10.1016/S0012-
1022 821X(03)00425-4.
1023 Dupont P., 2015. Compte rendu d'acquisition sismique. Campagne GHASS. N/O Pourquoi
1024 Pas ?, 1 Septembre - 30 Septembre 2015. PDG/REM/GM/EIS-30092015-01.

1025 Egorov, V. N., Artemov, Y. G., Gulin, S.B., Polikarpov G.G., 2011. Methane seeps in the
1026 Black Sea: discovery, quantification and environmental assessment. J. Black
1027 Sea/Mediterranean Environment. 17, 171-185.
1028 Egorov, V., Luth, U., Luth, C., Gulin, M.B., 1998. Gas seeps in the submarine Dnieper
1029 Canyon, Black Sea: acoustic, video and trawl data, in: Luth, U., Luth, C., Thiel, H.
1030 (Eds.), Methane Gas Seep Explorations in the Black Sea (MEGASEEBS). Project
1031 Report. Zentrum für Meres-und Klimaforschung, Universität Hamburg, Hamburg, pp.
1032 11-21.
1033 Field, M.E., Barber, J.H., 1993. A submarine landslide associated with shallow seafloor gas
1034 and gas hydrates off northern California, in: Schwab, W.C., Lee, H.J., Twichell, D.C.
1035 (Eds.), Submarine landslides: selected studies in the U.S. Exclusive Economic Zone.
1036 U.S. Geological Survey.
1037 Finetti, I., Bricchi, G., Del Ben, A., Pipan, M. and Xuan, Z., 1988. Geophysical study of the
1038 Black Sea. Bollettino di Geofisica Teorica ed Applicata. 30, 117-118, 197-324.
1039 Garziglia, S., Migeon, S., Ducassou, E., Loncke, L., Mascle, J., 2008. Mass-transport
1040 deposits on the Rosetta province (NW Nile deep-sea turbidite system, Egyptian
1041 margin): characteristics, distribution, and potential causal processes. Marine Geology.
1042 250, 180-198. https://doi.org/10.1016/j.margeo.2008.01.016.
1043 Georgiev, G., 2012. Geology and hydrocarbon Systems in the Western Black Sea. Turk. J.
1044 Earth Sci. 21, 723-754.
1045 Gillet, H., Lericolais, G., Réhault, J.-P., 2007. Messinian event in the black sea: Evidence of
1046 a Messinian erosional surface. Marine Geology. 244, 142-165.
1047 https://doi.org/10.1016/j.margeo.2007.06.004.
1048 Görür, N., 1988. Timing of opening of the Black Sea basin. Tectonophysics. 147, 247- 262.
1049 https://doi.org/10.1016/0040-1951(88)90189-8.
1050 Greinert, J., McGinnis, D. F., Naudts, L., Linke, P., De Batist, M., 2010. Atmospheric
1051 methane flux from bubbling seeps: spatially extrapolated quantification from a Black
1052 Sea shelf area, J. Geophys. Res.: Oceans. 115. https://doi.org/10.1029/2009JC005381.

1053 Haq, B.U., 1998. Natural gas hydrates: Searching the long-term climatic ans slope stability
1054 records, in: Henriet, J.P. and Miniert, J., (Eds), Gas hydrates: Relevance to world
1055 margin stability and climatic change: Geological Society (London) Special Publication
1056 137, 303-318. https://doi.org/10.1144/GSL.SP.1998.137.01.24.
1057 Hillman, J. I. T., Klaucke, I., Bialas, J., Feldman, H., Drexler, T., Awwiller, D., Atgin, O., Çifçi,
1058 G., Badhani, S., 2018. Gas migration pathways and slope failures in the Danube Fan,
1059 Black Sea. Marine and Petroleum Geology. 92, 1069-1084.
1060 https://doi.org/10.1016/j.marpetgeo.2018.03.025.
1061 Hippolyte, J-C., 2002. Geodynamics of Dobrogea (Romania): new constraints on the
1062 evolution of the Tornquist-Teysseyre Line, the Black Sea and the Carpathians.
1063 Tectonophysics. 357, 33-53. https://doi.org/10.1016/S0040-1951(02)00361-X.
1064 Hsü, K.J., Giovanoli, F., 1979. Messinian event in the black sea. Palaeogeography,
1065 Palaeoclimatology, Palaeoecology. 29, 75-93. https://doi.org/10.1016/0031-
1066 0182(79)90075-0.
1067 International Seismological Centre (2020), On-line Bulletin,
1068 https://doi.org/10.31905/D808B830.
1069 Ion, G., Lericolais, G., Nouzé, H., Panin, N., Ion, E. 2001. Seismo-acoustics evidence of
1070 gases in sedimentary edifices of the paleo-Danube realm, in: Turbidite systems and
1071 deep-sea fans of the Mediterranean and the Black seas. CIESM Workshop Series, 17,
1072 91-95. Bucharest (Romania), 5 - 8 June 2002, 119 p.
1073 Kennett, J.P., Cannariato, K.G., Hendy, I.L., Behl, R.J., 2003. Methane hydrates in
1074 Quaternary climate change: The clathrate gun hypothesis: Washington, D.C., American
1075 Geophysical Union. 213. https://doi.org/10.1002/9781118665138.ch0.
1076 Ker, S., Riboulot, V., 2015. GHASS cruise Team (2015). GHASS cruise report.
1077 https://archimer.ifremer.fr/doc/00300/41141/.
1078 Ker, S., Thomas, Y., Riboulot, V., Sultan, N., Bernard, C., Scalabrin, C., Ion, G., Marsset, B.,
1079 2019. Anomalously Deep BSR Related to a Transient State of the Gas Hydrate System

in the Western Black Sea. Geochemistry, Geophysics, Geosystems. 20, 442-459. https://doi. org/10.1029/2018GC007861.

Kim, Y-G., Lee, S-M., Jin, Y.K., Baranov, B., Obzhirov, A., Salomatin, A., Shoji, H., 2013. The stability of gas hydrate field in the northeastern continental slope of Sakhalin Island, Sea of Okhotsk, as inferred from analysis of heat flow data and its implications for slope failures. Marine and Petroleum Geology. 45, 198-207. https://doi.org/10.1016/j.marpetgeo.2013.05.003.

Knox, G.J., Omatsola, E.M., 1989. Development of the Cenozoic Niger delta in terms of the "escalator regression" model and impact on hydrocarbon distribution. Koninklijk Nederlands Geologisch en Mijnbouwkundig Gezelschap Symposium on Coastal Lowlands, Geology and Geotechnology Proceeding (1987). Kluwer Academic Publishers, Dortrecht, Netherlands, 181-202. doi:10.1007/978-94-017-1064-0_12.

Konerding, C., Dinu, C., Wong, H.K., 2010. Seismic sequence stratigraphy, structure and subsidence history of the Romanian Black Sea shelf, in: Sosson, M., Kaymakci, N., Stephenson, R.A., Bergerat, F., Starostenko, V., (Eds.), Sedimentary Basin Tectonics from the Black Sea and Caucasus to the Arabian Platform. Journal of the Geological Society, London, Special Publications, 340, pp. 159-180. https://doi.org/10.1144/SP340.9.

Krezsek, C., Schleder, Z., Bega, Z., Ionescu, G., Tari, G., 2016. The Messinian sea-level fall in the western Black Sea: small or large? Insights from offshore Romania. Pet. Geosci. 22, 392–399. https://doi.org/10.1144/petgeo2015-093.

Krézsek, C., Olariu, C., 2021. Filling of sedimentary basins and the birth of large rivers: The lower Danube network in the Dacian Basin, Romania. Global and Planetary Change. 197. doi.org/10.1016/j.gloplacha.2020.103391.

Kruglyakova, R.P., Byakov, Y.A., Kruglyakova, M.V., Chalenko, L.A., Shevtsova, N.T., 2004. Natural oil and gas seeps on the Black Sea floor. Geo Mar. Lett. 24, 150-162. DOI 10.1007/s00367-004-0171-4.

1107 Kvenvolden, K.A., 1993. Gas hydrates-Geological perspective and global change. Rev.
1108 Geophys. 31, 173-187. https://doi.org/10.1029/93RG00268.
1109 Kvenvolden, K.A., and McMenamin M.A., 1980. Hydrates of natural gas: A review of their
1110 geologic occurrence. U.S. Geol. Survey Circ. C825, 11.
1111 Kwon, T.H., Cho, G.C., 2012. Submarine slope failure primed and triggered by bottom water
1112 warming in oceanic hydrate-bearing deposits. Energies. 5, 2849-2873.
1113 https://doi.org/10.3390/en5082849.
1114 Lafuerza, S., Sultan, N., Canals, M., Frigola, J., Berné, S., Jouet, G., Galavazi, M., Sierro,
1115 F.J., 2009. Overpressure within upper continental slope sediments from CPTU data,
1116 Gulf of Lion, NW Mediterranean Sea. International Journal of Earth Sciences. 98, 4,
1117 751-768. https://doi.org/10.1007/s00531-008-0376-2.
1118 Lee, H.J., 2005. Undersea landslides: extent and significance in the Pacific Ocean, an
1119 update. Nat. Hazards Earth Syst. Sci. 5, 877-892. https://doi.org/10.5194/nhess-5-877-
1120 2005.
1121 Lericolais, G., Bourget, J., Popescu, I., Jermannaud, P., Mulder, T., Jorry, S., Panin, N.,
1122 2013. Late Quaternary deep-sea sedimentation in the western Black Sea: new insights
1123 from recent coring and seismic data in the deep basin. Global Planet. Change. 103,
1124 232-247. https://doi.org/10.1016/j.gloplacha.2012.05.002.
1125 Lericolais, G., Bulois, C., Gillet, H., Guichard, F., 2009. High frequency sea level fluctuations
1126 recorded in the Black Sea since the LGM. Glob. Planet. Chang. 66, 65-75.
1127 https://doi.org/10.1016/j.gloplacha.2008.03.010.
1128 Letouzey, J., Biju-Duval, B., Dorkel, A., Gonnard, R., Kristchev, K., Montadert, L., Sungurlu,
1129 O., 1977. The Black Sea: a marginal basin: geophysical and geological data, in: Biju-
1130 Duval, B., Montadert,L. (Eds.), Structural History of the Mediterranean Basins. Editions
1131 Technip, Paris, pp. 363-376.
1132 Locat, J., Leroueil, S., Locat, A., Lee, H., 2014. Weak Layers: Their definition and
1133 classification from a geotechnical perspective, in:Krastel S., Behrmann, J.H., Völker, D.,
1134 Stipp, M., Berndt, C., Urgele, R., et al. (Eds.), Submarine Mass Movements and Their

Consequences. Advances in Natural and Technological Hazards Research. 37, Springer, Cham, Switzerland, pp. 3-12.

Løvholt, F., Glimsdal, S., Harbitz, C.B., 2020. On the landslide tsunami uncertainty and hazard. Landslide. 17, 2301-2315.Madof, A.S., Christie-Blick, N., Anders, M.H., 2009. Stratigraphic controls on a salt-withdrawal intraslope minibasin, north-central Green Canyon, Gulf of Mexico: Implications for misinterpreting sea level change. AAPG Bull. 93, 4, 535–561. DOI:10.1306/12220808082.

Magara, K., 1978. Compaction and fluid migration. Practical petroleum geology. Developments in Petroleum Science. 9, 11-46.

Marsset, B., Menut, E., Ker, S., Thomas, Y., Regnault, J.P., Leon, P., Martinossi, H., Artzner, L., Chenot, D., Dentrecolas, S., Spychalski, B., Mellier, G., Sultan, N., 2014. Deep-towed high resolution multichannel seismic imaging, Deep Sea Res., Part I: Oceanogr. Res. Pap. 93, 83–90. https://doi.org/10.1016/j.dsr.2014.07.013.

Marsset, B., Ker, S., Thomas, Y., Colin, F., 2018. Deep-towed high resolution seismic imaging II: Determination of P-wave velocity distribution, Deep Sea Res., Part I-oceanographic Res. Pap. 132, 29–36. https://doi.org/10.1016/j.dsr.2017.12.005.

Marsset, T., Marsset, B., Ker, S., Thomas, Y., Le Gall, Y., 2010. High and very resolution deep-towed seismic system: performance and examples from deep water geohazard studies. Deep Sea Res. I. 57, 4, 628–637. https://doi.org/10.1016/j.dsr.2010.01.001.

Martinez-Lamas, R., Toucanne, S., Debret, M., Riboulot, V., Deloffre, J., Boissier, A., Cheron, S., Pitel, M., Bayon, G., Giosan, L., Soulet, G., 2020. Linking Danube River activity to Alpine Ice-Sheet fluctuations during the last glacial (ca. 33–17 ka BP): Insights into the continental signature of Heinrich Stadials. Quaternary Science Reviews. 229, 106136. https://doi.org/10.1016/j.quascirev.2019.106136.

Maslin, M.A., Mikkelsen, N., Vilela, C., and Haq, B., 1998. Sea-level- and gas-hydrate-controlled catastrophic sediment failures of the Amazon Fan: Geology, 26, 12, 1107-1100. https://doi.org/10.1130/0091-7613(1998)026<1107:SLAGHC>2.3.CO;2.

1162 Maslin, M., Owen, M., Day, S., Long., D., 2004. Linking continental-slope failures and climate
1163 change: Testing the clathrate gun hypothesis. Geology, 32,1, 53-56.
1164 https://doi.org/10.1016/j.dsr.2014.07.013.
1165 Masson, D.G., Harbitz, C.B., Wynn, R.B., Pedersen, G., Løvholt, F., 2006. Submarine
1166 landslides: processes, triggers, and hazard prediction. Phil. Trans. R. Soc. A. 364,
1167 2009-2039. https://doi.org/10.1098/rsta.2006.1810.
1168 Matenco, L., Munteanu, I., Ter Borgh, M., Stanica, A., Tilita, M., Lericolais, G., Dinu C., Oaie
1169 G., 2016. The interplay between tectonics, sediment dynamics and gateways evolution
1170 in the Danube system from the Pannonian Basin to the western Black Sea. Science Of
1171 The Total Environment. 543, 807-827. Publisher's official version
1172 https://doi.org/10.1016/j.scitotenv.2015.10.081.
1173 Matoshko, A., Matoshko, A., de Leeuw, A., 2019. The Plio-Pleistocene demise of the East
1174 Carpathians foreland fluvial system and arrival of the Paleo-Danube to the Black Sea.
1175 Geol. Carpath. 70, 2, 91-112. https://doi.org/10.2478/geoca-2019-0006.
1176 Matova, M., 2000. Recent geological activity along the northeastern Bulgarian Black Sea
1177 coast. Geol. Quaterly. 44, 355-362.
1178 Merey, S., and Sinayuc, C., 2016. Investigation of gas hydrate potential of the Black Sea and
1179 modelling of gas production from a hypothetical Class 1 methane hydrate reservoir in
1180 the Black Sea conditions, J. Nat. Gas Sci. Eng. 29, 66-79.
1181 https://doi.org/10.1016/j.jngse.2015.12.048.
1182 Mitchum, R.M., Vail, P.R., 1977. Seismic stratigraphy and global changes in sea-level, part 7:
1183 stratigraphic interpretation of seismic reflection patterns in depositional sequences, in:
1184 Payton, C.E. (Ed.), Seismic Stratigraphy - Applications to Hydrocarbon Exploration.
1185 AAPG Memoir. Tulsa, 26, pp. 135–144.
1186 Mitchum, R.M., Vail, P.R., Sangree, J.B., 1977. Seismic stratigraphy and global changes in
1187 sea-level, part 6: seismic stratigraphic interpretation procedure, in: Payton, C.E. (Ed.),
1188 Seismic Stratigraphy - Applications to Hydrocarbon Exploration. AAPG Memoir. Tulsa,
1189 26, pp. 117–134.

1190 Morosanu, I., 2007. Romanian continental plateau of the Black Sea, Oscar print, Bucharest,
1191 176 pp, ISBN 078-973-668-167-7.
1192 Munteanu, I., Matenco, L., Dinu, C., Cloetingh, S., 2011. Kinematics of back-arc inversion of
1193 the Western Black Sea Basin. Tectonics. 30, TC5004. http://dx.doi.org/10.1029/
1194 2011tc002865.
1195 Munteanu, I., Matenco, L., Dinu, C., Cloetingh, S., 2012. Effects of large sea-level variations
1196 in connected basins: the Dacian-Black Sea system of the Eastern Paratethys. Basin
1197 Res. 24, 583-597. https://doi.org/10.1111/j.1365-2117.2012.00541.x.
1198 Naudts, L., Greinert, J., Artemov, Y., Staelens, P., Poort, J., Van Rensbergen, P., De Batist,
1199 M., 2006. Geological and morphological setting of 2778 methane seeps in the Dnepr
1200 paleo delta, northwestern Black Sea. Mar. Geol. 227, 177-199,
1201 doi:10.1016/j.margeo.2005.10.005.
1202 Naudts, L., Greinert, J., Artemov, Y., Beaubien, S.E., Borowski, C., De Batist, M., 2008.
1203 Anomalous sea-floor backscatter patterns in methane venting areas, Dnepr paleo-delta,
1204 NW Black Sea. Mar. Geol. 251, 253-267. https://doi.org/10.1016/j.margeo.2008.03.002.
1205 Nikishin, A.M., Ziegler, P.A., Panov, D.I., Nazarevich, B.P., Brunet, M-F., Stephenson, R.A.,
1206 Bolotov, S.N., Korotaev, M.V. & Tikhomirov, P.L. 2001. Mesozoic and Cainozoic
1207 evolution of the Scythian Platform-Black Sea-Caucasus domain, in: Ziegler, P.A.,
1208 Cavazza, W., Robertson, A.H.F., Crasquin-Soleau, S. (Eds.), Peri-Tethys Memoir, 6:
1209 Peri-Tethyan Rift /Wrench Basins and Passive Margins. Memoires du Museum National
1210 d`Histoire Naturelle, 186, 295-346.
1211 Nikishin, A., Ziegler, P., Bolotov, S.N. and Fokin, P.A., 2011. Late Palaeozoic to Cenozoic
1212 Evolution of the Black Sea-Southern Eastern Europe Region: A View from the Russian
1213 Platform. Turkish Journal of Earth Science. 20, 571-634.
1214 Nikolovska, A., H. Sahling, and G. Bohrmann, 2008. Hydroacoustic methodology for
1215 detection, localization, and quantification of gas bubbles rising from the seafloor at gas
1216 seeps from the eastern Black Sea, Geochem. Geophys. Geosyst. 9, Q10010,
1217 doi:10.1029/2008GC002118.

1218 Panin, N., Jipa, D., 2002. Danube River Sediment Input and its Interaction with the North-
1219 western Black Sea Estuarine, Coastal and Shelf Science 54, 551-562,
1220 doi:10.1006/ecss.2000.0664.
1221 Panin, N., Panin, S., Herz, N., Noakes, J. E., 1983. Radiocarbon dating of Danube delta
1222 deposits. Quaternary Research. 19, 249-255. https://doi.org/10.1016/0033-
1223 5894(83)90008-X.
1224 Papadopoulos, G. A., Diakogianni, G., Fokaefs, A., Ranguelov, B., 2011. Tsunami hazard in
1225 the Black Sea and the Azov Sea: a new tsunami catalogue. Nat. Hazards Earth Syst.
1226 Sci. 11, 945–963. https://doi:10.5194/nhess-11-945-2011.
1227 Pătruț, I., Paraschiv, C., Dăneț, T., Balteș, N., Dăneț, N., Motaș, L., 1984. The Geological
1228 constitution of the Danube Delta. Anuarul Institutului de Geologie și Geofizică -
1229 Annuaire de l'Institut de Géologie et de Géophysique. 59, 55-61.
1230 Pecher, I.A., Henrys, S.A., Ellis, S., Chiswell, S.M., Kukowski, N., 2005. Erosion of the
1231 seafloor at the top of the gas hydrate stability zone on the Hikurangi Margin, New
1232 Zealand. Geophysical Research Letters. 32, 24.
1233 https://doi.org/10.1029/2005GL024687.
1234 Piper, D. J. W., C. Pirmez, P. L. Manley, D. Long, R. D. Flood, W. R. Normark and W.
1235 Showers, 1997. Mass-transport deposits of the Amazon Fan, in: Flood, R. D., Piper, D.
1236 J. W., Klaus, A., Peterson, L. C. (Eds.), Proceedings of the Ocean Drilling Program:
1237 Scientific Results, 155, 109-146: College Station, Texas (Ocean Drilling Program).
1238 Piper, D.J.W., Cochonat, P., Morrison, M.L., 1999. The sequence of events around the
1239 epicentre of the 1929 Grand Banks earthquake: initiation of debris flows and turbidity
1240 current inferred from sidescan sonar. Sedimentology. 46, 79-97.
1241 https://doi.org/10.1046/j.1365-3091.1999.00204.x.
1242 Polikarpov, G.G., Egorov, V.N., Nezhdanonv, A.I., Gulin, S.B., Kulev, Y.D., Gulin, M.B.,
1243 1989. Methane gas seeps in the Black Sea—a new object of molismology, in:
1244 Polikarpov, G.G. (Ed.), Molismology of the Black Sea. Nauka, Kiev, pp. 10-20.

1245 Pope, E.L., Talling, P.J., Carter, L., 2017. Which earthquakes trigger damaging submarine
1246 mass movements: Insights from a global record of submarine cable breaks? Mar. Geol.
1247 384, 131-146. https://doi.org/10.1016/j.margeo.2016.01.009.
1248 Popescu, I., 2002. Analyse des processus sédimentaires récents dans l'éventail profond du
1249 Danube (Mer Noire). PhD thesis, Universit~é de Bretagne Occidentale. 282 pp.
1250 Popescu, I., De Batist, M., Lericolais, G., Nouze, H., Poort, J., Panin, N., Versteeg, W., Gillet,
1251 H., 2006. Multiple bottom-simulating reflections in the Black Sea: potential proxies of
1252 past climate conditions. Mar. Geol. 227, 163-176. https://
1253 doi.org/10.1016/j.margeo.2005.12.006.
1254 Popescu, I., Lericolais, G., Panin, N., De Batist, M., Gillet, H., 2007. Seismic expression of
1255 gas and gas hydrates across the western Black Sea. Geo-Marine Letters. 27, 173-183.
1256 https://doi.org/10.1007/s00367-007-0068-0.
1257 Popescu, I., Lericolais, G., Panin, N., Normand, A., Dinu, C., Le Drezen, E., 2004. The
1258 Danube submarine canyon (Black Sea): morphology and sedimentary processes. Mar.
1259 Geol. 206, 249-265. https://doi.org/10.1016/j.margeo.2004.03.003.
1260 Popescu, I., Lericolais, G., Panin, N., Wong, H.K., Droz, L., 2001. Late Quaternary channel
1261 avulsions on the Danube deep-sea fan. Black Sea. Mar. Geol. 179, 25- 37.
1262 https://doi.org/10.1016/S0025-3227(01)00197-9.
1263 Posamentier, H. W., Kolla, V., 2003. Seismic geomorphology and stratigraphy of depositional
1264 elements in deep-water settings: Journal of Sedimentary Research. 73, 367-388,
1265 doi:10.1306/111302730367.
1266 Riboulot, V., Cattaneo, A., Scalabrin, C., Gaillot, A., Jouet, G., Ballas, G., Marsset, T.,
1267 Garziglia, S., Ker, S., 2017. Control of the geomorphology and gas hydrate extent on
1268 widespread gas emissions offshore Romania. Bull. Soc. Geol. Fr. 188 (4), 26.
1269 https://doi.org/10.1051/bsgf/2017182.
1270 Riboulot, V., Cattaneo, A., Sultan, N., Garziglia, S., Ker, S., Imbert, P., Voisset, M., 2013.
1271 Sea-level change and free gas occurrence influencing a submarine landslide and

1272 pockmark formation and distribution in deepwater Nigeria. Earth Planet. Sci. Lett. 375,
1273 78-91. https://doi.org/10.1016/j.epsl.2013.05.013.
1274 Riboulot, V., Ker, S., Sultan, N., Thomas, Y., Marsset, B., Scalabrin, C., Ruffine, L., Boulart,
1275 C., Ion, G., 2018. Freshwater lake to salt-water sea causing widespread hydrate
1276 dissociation in the Black Sea, Nat. Commun. 9 (117).
1277 https://doi.org/10.1016/j.epsl.2013.05.013.
1278 Robinson, A.G., Rudat, J.H., Banks, C.J., Wiles, R.L.F., 1996. Petroleum geology of the
1279 Black Sea. Mar. Pet. Geol. 13, 195-223. https://doi.org/10.1016/0264-8172(95)00042-9.
1280 Römer, M., Sahling, H., dos Santos Ferreira, C., Bohrmann, G., 2020. Methane gas
1281 emissions of the Black Sea-mapping from the Crimean continental margin to the Kerch
1282 Peninsula slope. Geo-Marine Letters. 40, 467-480. https://doi.org/10.1007/s00367-019-
1283 00611-0.
1284 Rouby, D., Nalpas T., Jermannaud P., Robin C., Guillocheau F., Raillard S., 2011. Gravity
1285 driven deformation controlled by the migration of the delta front: The Plio-Pleistocene of
1286 the Eastern Niger Delta. Tectonophysics. 513, 54-67. doi:
1287 https://doi.org/10.1130/GEOSO1426.1.
1288 Schleder, Z., Krezsek, C., Lapadat, A., Bega, Z., Ionescu, G., Tari, G., 2016. Structural style
1289 in a Messinian (intra-Pontian) gravity-driven deformation system, western Black Sea,
1290 offshore Romania. Petroleum Geoscience. 22(4), 400-410.
1291 https://doi.org/10.1144/petgeo2015-094.
1292 Skarke A., Ruppel, C., Kodis, M., Brothers, D., Lobecker, E., 2014. Widespread methane
1293 leakage from the sea floor on the northern US Atlantic margin. Nature Geoscience.
1294 DOI :10.1038/NGEO2232.
1295 Sloan, E.D., Jr., Clathrate Hydrates of Natural Gases. 641 p. Marcel Dekker, New-York,
1296 1990.
1297 Sloan, E.D., Jr., Clathrate Hydrates of Natural Gases, 2 ed., 705 p., Marcel Dekker, New-
1298 York, 1998.

1299 Soulet, G., Ménot, G., Bayon, G., Rostek, F., Ponzevera, E., Toucanne, S., Lericolais, G.,
1300 Bard, E., 2013. Abrupt drainage cycles of the Fennoscandian Ice Sheet. PNAS. 110,
1301 17, 6682-6687. https://doi.org/10.1073/pnas.1214676110.
1302 Soulet, G., Ménot, G., Garreta, V., Rostek, F., Zaragosi, S., Lericolais, G., Bard, E., 2011.
1303 Black Sea "Lake" reservoir age evolution since the last glacial — hydrologic and
1304 climatic implications. Earth Planet. Sci. Lett. 308, 245-258.
1305 https://doi.org/10.1016/j.epsl.2011.06.002.
1306 Sultan, N., Cochonat, P., Canals, M., Cattaneo, A., Dennielou, B., Haflidason, H., Laberg,
1307 J.S., Long, D., Mienert, J., Trincardi, F., Urgeles, R., Vorren, T.O., Wilson, C., 2004a.
1308 Triggering mechanisms of slope instability processes and sediment failures on
1309 continental margins: a geotechnical approach. Mar.Geol. 213, 291–321.
1310 https://doi.org/10.1016/j.margeo.2004.10.011.
1311 Sultan, N., Cochonat, P., Foucher, J.-P., Mienert, J., 2004b. Effect of gas hydrates melting
1312 on seafloor slope instability. Mar. Geol. 213, 379-401.
1313 https://doi.org/10.1016/j.margeo.2004.10.015.
1314 Tailling, P.J., Clare, M., Urlaub, M., Pope, E., Hunt, J.E., Watt, S.F.L., 2014. Large
1315 submarine landslides on continental slopes: Geohazards, methane release, and climate
1316 change. Oceanography. 27, 2, 32-45. http://www.jstor.org/stable/24862153.
1317 Ţambrea, D., 2007. Subsidence analysis and tectonic-thermal evolution of the Istria
1318 Depression (Black Sea); Implications for the hydrocarbon generation (in Romanian).
1319 Ph.D thesis, Bucharest University, 156 p.
1320 Tambrea, D., Dinu, C., Sampetrean, E., 2002. Characteristics of the Tectonics and
1321 Lithostratigraphy of The Black Sea Shelf, Offshore Romania, in: Dinu, C., Mocanu, V.
1322 (Eds.), Geology and Tectonics of the Romanian Black Sea Shelf and its Hydrocarbon
1323 Potential. Vergiliu, Bucharest, pp. 29-42.
1324 Twichell, D. C., Kenyon, N. H., Parson, L. M., McGregor, B. A., 1991. Depositional patterns
1325 of the Mississippi Fan surface: Evidence from GLORIA II and high-resolution seismic
1326 profiles, in: Weimer, P. and Link, M. H. (Eds.), Seismic facies and sedimentary

processes of submarine fans and turbidite systems. Frontiers in Sedimentary Geology. Springer-Verlag, New York, pp. 349-363. https://doi.org/10.1007/978-1-4684-8276-8_19.

Urlaub, M., Talling, P.J., Masson, D.G., 2013. Timing and frequency of large submarine landslides: implications for understanding triggers and future geohazard. Quaternary Science Reviews. 72, 63-82. https://doi.org/10.1016/j.quascirev.2013.04.020.

Vail, P.R., Mitchum Jr., R.M., Thompson, S.I.I.I., 1977. Seismic stratigraphy and global changes of sea level, part 4, global cycles of relative changes of sea level, in: Payton, C.E. (Ed.), Seismic Stratigraphy - Applications to Hydrocarbon Exploration. American Association of Petroleum Geologists, Memoir 26, 83-97.

Van Wagoner, J.C., Posamentier, H.W., Mitchum, R.M., Vail, P.R., Sarg, J.F., Loutit, T.S., Hardenbol, J., 1988. An overview of the fundamentals of sequence stratigraphy and key definitions, in: Wilgus, C.K., Hastings, B.S., Kendall, C.G., Posamentier, H.W., Ross, C.A., Van Wagoner, J.C. (Eds.), Sea Level Changes: an integrated approach. SEPM, 42, pp. 39-45.

Wegwerth, A., Ganopolski, A., Ménot, G., Kaiser, J., Dellwig, O., Bard, E., Lamy, F., Arz, H.W., 2015. Black Sea temperature response to glacial millennial-scale climate variability. Geophys. Res. Lett. 42, 8147-8154. https://doi.org/10.1002/2015GL065499.

Weimer, P., 1990. Sequence stratigraphy, facies geometries, and depositional history of the Mississippi fan, Gulf of Mexico. AAPG Bull. 74 (4), 425-453. https://doi.org/10.1306/0C9B2321-1710-11D7-8645000102C1865D.

Winguth, C., Wong, H.K., Panin, N., Dinu, C., Georgescu, P., Ungureanu, G., Krugliakov, V.V., Podshuveit, V., 2000. Upper quaternary water level history and sedimentation in the northwestern Black Sea. Mar. Geol. 167, 127- 146. https://doi.org/10.1016/S0025-3227(00)00024-4.

Yilmaz, Y., Tuysuz, O., Yigitbas, E., Genc, S.C., Sengor, A.M.C., 1997. Geology and Tectonic Evolution of the Pontides, in: Robinson A.G. (Ed.), Regional and Petroleum Geology of the Black Sea and Surrounding Region. AAPG Memoir, 68, 183-226.

1355 Yang, J., Davies, R., 2013. Gravity-driven faults: migration pathways for recycling gas after
1356 the dissociation of marine gas hydrates. Marine Geology 336, 1-9.
1357 https://doi.org/10.1016/j.margeo.2012.11.013.
1358 Zander, T., Haeckel, M., Berndt, C., Chi, W.C., Klaucke, I., Bialas, J., Klaeschen, D., Koch,
1359 S., Atgın, O., 2017. On the origin of multiple BSRs in the Danube deep-sea fan, Black
1360 Sea. Earth Planet. Sci. Lett. 462, 15-25. https://doi.org/10.1016/j.epsl.2017.01.006.
1361 Zonenshain, L.P., Le Pichon, X., 1986. Deep basins of the Black Sea and Caspian Sea as
1362 remnants of Mesozoic back-arc basins. Tectonophysics. 123, 181-212.
1363 https://doi.org/10.1016/0040-1951(86)90197-6.
1364